Article

Balanced plant helper NLR activation by a modified host protein complex

https://doi.org/10.1038/s41586-024-08521-7

Received: 24 April 2024

Accepted: 12 December 2024

Published online: 12 February 2025

Check for updates

Shijia Huang[1,2,8], Junli Wang[3,8], Ridan Song[4,8], Aolin Jia[5,8], Yu Xiao[4], Yue Sun[1,2], Lin Wang[1,2], Dennis Mahr[3], Zhongshou Wu[6], Zhifu Han[1,2], Xin Li[6], Jane E. Parker[3,7]✉ & Jijie Chai[1,2]✉

Nucleotide-binding leucine-rich repeat (NLR) receptors play crucial roles in plant immunity by sensing pathogen effectors[1]. In *Arabidopsis*, certain sensor NLRs function as NADases to catalyse the production of second messengers[2,3], which can be recognized by enhanced disease susceptibility 1 (EDS1) with its partner senescence-associated gene 101 (SAG101), to activate helper NLR N requirement gene 1 (NRG1)[4]. A cryoelectron microscopy structure shows that second-messenger-activated EDS1–SAG101 mainly contacts the leucine-rich repeat domain of NRG1A to mediate the formation of an induced EDS1–SAG101–NRG1A complex. Structural comparisons show that binding of a second messenger induces conformational changes in EDS1–SAG101, which are recognized by NRG1A, leading to its allosteric activation. We further show that an inhibitory NRG1 family member, NRG1C, efficiently outcompetes NRG1A for binding to second-messenger-activated EDS1–SAG101. These findings uncover mechanisms for NRG1A activation through its recognition of a modified host EDS1–SAG101 complex, and NRG1A inhibition by NRG1C through sequestration of the activated EDS1–SAG101, thus shedding light on the activation and constraint of a central plant immune response system.

Plant immunity is a sophisticated system that enables plants to recognize and defend against various potentially harmful pathogens[1,5]. This system is primarily mediated by two types of immune receptor: (1) cell surface pattern recognition receptors that perceive pathogen-associated molecular patterns and host-derived damage-associated molecular patterns and (2) intracellular nucleotide-binding leucine-rich repeat (NLR) receptors[6]. NLRs directly or indirectly detect strain-specific pathogen effector proteins delivered into the plant cell, leading to the activation of effector-triggered immunity (ETI). ETI is frequently accompanied by a hypersensitive response, a form of localized programmed cell death associated with pathogen restriction[7]. One model that explains the indirect recognition mode is known as the 'guard hypothesis', in which an NLR protein senses effector-mediated modifications of a host target protein, termed a 'guardee'[8,9].

NLRs are generally composed of a conserved central nucleotide-binding and oligomerization (NOD) module, an N-terminal signalling domain and a C-terminal leucine-rich repeat (LRR) domain typically responsible for effector recognition. NLRs can be categorized into different subfamilies based on their N-terminal coiled-coil (CC), Toll/interleukin-1 receptor (TIR) or resistance to powdery mildew 8-like CC domains, which are termed CNLs, TNLs and RNLs, respectively[10,11]. Whereas sensor NLRs (sNLRs) are responsible for the recognition of pathogen effectors, RNLs function to translate signals from sNLRs into ETI or pattern-triggered immunity (PTI) responses and are therefore known as helper NLRs (hNLRs). Examples of hNLRs include *Arabidopsis thaliana*-activated disease resistance 1 (*At*ADR1) and N requirement gene 1 (*At*NRG1), and NLRs required for cell death (NRCs) in *Solanaceae*. Direct or indirect activation of NLRs by pathogen effectors leads to the formation of higher-order oligomeric complexes known as resistosomes[12]. Pentameric[13–15] or hexameric[16] CNL and RNL[17,18] resistosomes possess Ca^{2+}-permeable ion channel activity that is required for their ETI activation. By comparison, TNL resistosomes function as NADase holoenzymes[2,3], which catalyse the production of second messengers such as ADP-ribosylated ATP (ADPr-ATP)/ADPr-ADPR (di-ADPR) and 2′-(5′′-phosphoribosyl)-5′-adenosine monophosphate/diphosphate (pRib-AMP/ADP) to activate ETI responses[4,19].

In *Arabidopsis*, TNL signalling depends on the EDS1 family, consisting of enhanced disease susceptibility 1 (*At*EDS1) and its direct and mutually exclusive partners phytoalexin-deficient 4 (*At*PAD4) and senescence-associated gene 101 (*At*SAG101), and two RNL subfamilies of hNLRs, *At*ADR1s and *At*NRG1s[20] (hereafter referred to as EDS1, PAD4, SAG101, ADR1 and NRG1, respectively). Following TNL activation, ADPr-ATP or di-ADPR binds to EDS1–SAG101 and pRib-AMP or pRib-ADP to EDS1–PAD4 dimers, which respectively activate NRG1 and ADR1 (refs. 4,18,19,21,22). This results in two functionally distinct signalling branches: (1) EDS1–SAG101–NRG1, which promotes TNL-triggered ETI and host cell death, and (2) EDS1–PAD4–ADR1, which potentiates host PTI and ETI defences[23–28]. NRG1C is an N-terminally truncated member of the NRG1 family possessing only a winged-helix domain (WHD) and LRR domain, and specifically suppresses signalling of full-length

[1]Research Center for Industries of the Future and School of Life Sciences, Westlake University, Hangzhou, China. [2]Institute of Biology, Westlake Institute for Advanced Study, Westlake Laboratory of Life Sciences and Biomedicine, Hangzhou, China. [3]Department of Plant-Microbe Interactions, Max Planck Institute for Plant Breeding Research, Cologne, Germany. [4]School of Life Sciences, Tsinghua University, Beijing, China. [5]National Key Laboratory of Wheat and Maize Crop Science, CIMMYT-China Wheat and Maize Joint Research Centre, Agronomy College, Henan Agricultural University, Zhengzhou, China. [6]Michael Smith Laboratories, University of British Columbia, Vancouver, British Columbia, Canada. [7]Cluster of Excellence on Plant Sciences, Max-Planck Institute for Plant Breeding Research, Cologne, Germany. [8]These authors contributed equally: Shijia Huang, Junli Wang, Ridan Song, Aolin Jia. ✉e-mail: parker@mpipz.mpg.de; chaijijie@westlake.edu.cn

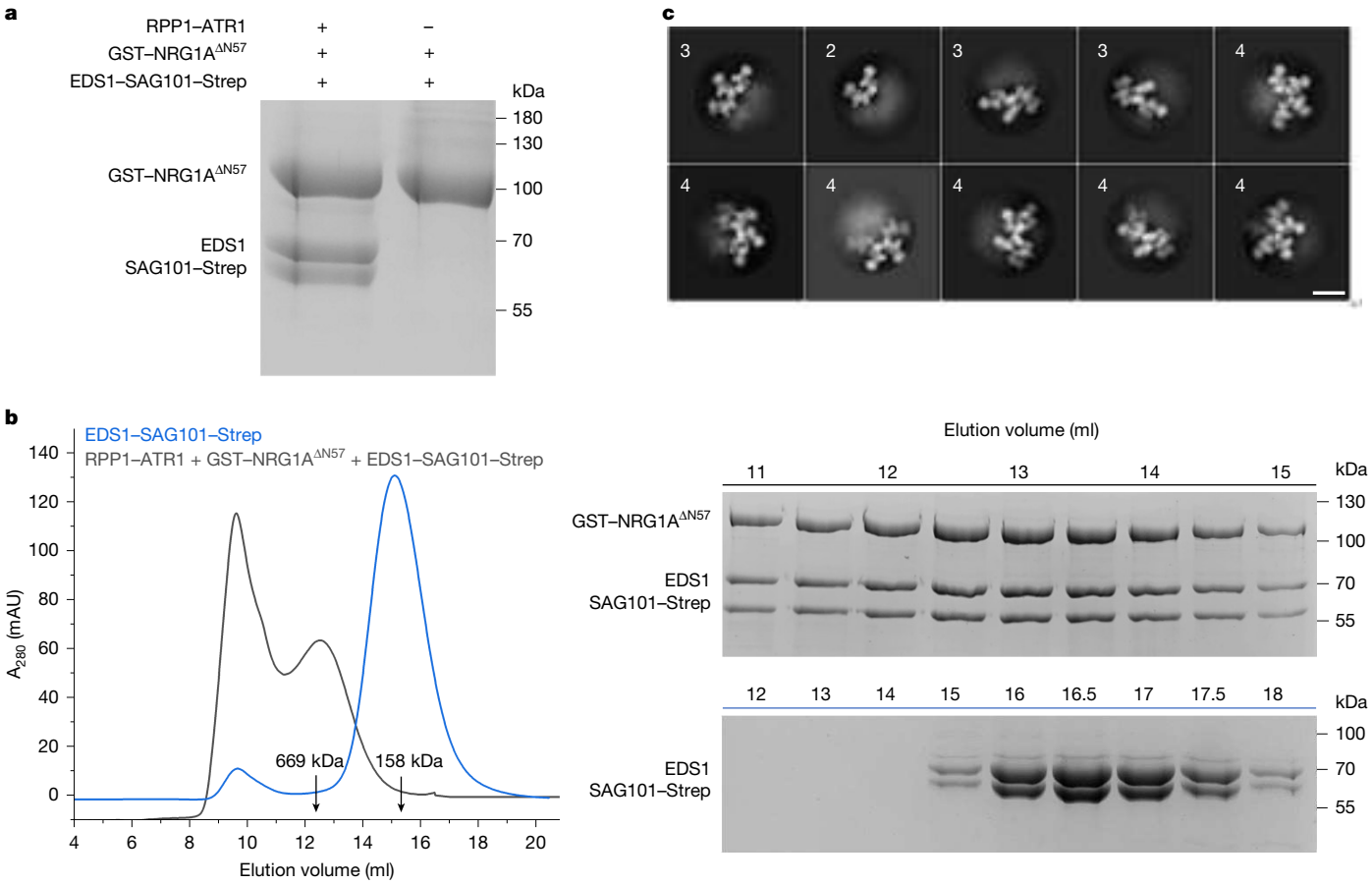

Fig. 1 | Induced oligomerization of EDS1–SAG101–NRG1A$^{\Delta N57}$. **a**, The RPP1 resistosome induces EDS1–SAG101 interaction with NRG1A$^{\Delta N57}$. N-terminally GST-tagged NRG1A$^{\Delta N57}$ was co-expressed with EDS1 and SAG101, with or without RPP1 and ATR1, in insect cells. GST beads were used for protein purification, and purified proteins were analysed by SDS–PAGE followed by staining with Coomassie brilliant blue. **b**, EDS1–SAG101–NRG1A$^{\Delta N57}$ (purified in **a**) forms oligomers in gel filtration (Superose 6 Increase 10/300). Left, gel filtration profiles of EDS1–SAG101 (blue) and EDS1–SAG101–NRG1A$^{\Delta N57}$ (black). EDS1–SAG101 with C-terminally tagged SAG101 was purified through Strep-tag affinity. Positions of standard molecular mass are indicated by arrows. Right, peak fractions in the left-hand panel were analysed by SDS–PAGE, followed by Coomassie brilliant blue staining. **a**,**b**, Experiments were repeated three times with similar results. For gel source data, see Supplementary Fig. 1. **c**, Representative views of two-dimensional class averages of the EDS1–SAG101–NRG1A$^{\Delta N57}$ complex purified in **b**. Heterotrimer numbers are indicated. Scale bar, 20 nm. A_{280}, absorbance at 280 nm; mAU, milli-absorbance units.

NRG1A/B forms, probably through interaction with the EDS1–SAG101 complex[29]. Expression of NRG1C is significantly induced in response to pathogen infection[29].

Structural and biochemical studies have elucidated the activation mechanisms of sNLRs[30]. Whereas NRC-type hNLRs were proposed to detect changes in sNLRs or sNLR-associated activities[31,32], ADR1- and NRG1-type hNLRs are directly activated by second-messenger-bound EDS1 dimers[33,34]. However, the mechanisms underlying the activation of hNLRs remain elusive. In this study, we demonstrate that ADPr-ATP is required for the EDS1–SAG101 heterodimer to interact with and induce NRG1A oligomerization. A cryoelectron microscopy (cryo-EM) structure of ADPr-ATP-bound EDS1–SAG101, in complex with an NRG1A variant (NRG1A$^{WHD\text{-}LRR}$, residues 391–809), shows that the C-terminal LRR domain mainly mediates NRG1A interaction with EDS1–SAG101; this is further confirmed by biochemical and in vivo functional analyses. Structural comparisons show that ADPr-ATP-induced conformational changes in the C-terminal 'EP' (EDS1–PAD4) domain of SAG101 are indispensable for EDS1–SAG101 interaction with NRG1A, supporting a critical role of the EDS1–SAG101 complex in the activation of NRG1A. Similar to pathogen effector proteins interacting with inactive sNLRs, EDS1–SAG101 clashes with the nucleotide-binding domain (NBD) of AlphaFold2-predicted inactive NRG1A to allosterically activate the hNLR. NRG1C completely overlaps with NRG1A when interacting with EDS1–SAG101, but exhibits higher EDS1–SAG101 binding affinity. NRG1C effectively outcompetes NRG1A for interaction with a TIR-catalysed, second-messenger-activated EDS1–SAG101 complex in vitro, leading to the sequestration of available EDS1–SAG101 and inhibition of NRG1A activation. These findings demonstrate the molecular mechanisms underlying the activation and negative regulation of a plant hNLR, filling an important gap in our understanding of EDS1 immune signalling.

Oligomerization of EDS1–SAG101–NRG1A

The *Arabidopsis* NRG1 subfamily comprises two full-length members, NRG1A and NRG1B, and an N-terminally truncated form, NRG1C. Because of the low expression level of full-length NRG1A in the insect expression system, we chose an NRG1A variant with 57 N-terminal residues deleted (termed NRG1A$^{\Delta N57}$) to investigate its activation mechanism, by co-expressing the RPP1 resistosome (containing RPP1 (residues 61–1,221) and its cognate effector ATR1), EDS1 and SAG101 in insect cells. In this co-expression system, RPP1 resistosome-catalysed second messengers (ADPr-ATP/di-ADPR) stimulate the interaction of EDS1–SAG101 with NRG1A[4]. A glutathione *S*-transferase (GST)-based pulldown assay showed a strong interaction between N-terminally GST-tagged NRG1A$^{\Delta N57}$ and EDS1–SAG101 (Fig. 1a and Extended Data Fig. 1a). Gel filtration analysis of the affinity-purified EDS1–SAG101–NRG1A$^{\Delta N57}$ protein indicated that the protein complex formed oligomers with a molecular weight around the standard marker of 669 kDa (Fig. 1b). By

comparison, the EDS1–SAG101 complex was eluted at position 158 kDa in this assay (Fig. 1b). These results suggest that EDS1–SAG101 binding leads to the formation of oligomeric EDS1–SAG101–NRG1A complexes, and are consistent with a previous study showing that EDS1–SAG101 remains associated with NRG1 following its activation[18]. In contrast, another investigation suggested that the NRG1A resistosome contains no EDS1 family proteins[35]. The reason for this discrepancy is unknown. Because we were unable to purify correctly folded NRG1A$^{\Delta N57}$ when expressed alone, it remains unclear whether the NRG1A$^{\Delta N57}$ protein was monomeric before EDS1–SAG101 binding.

To further characterize the gel filtration-purified oligomeric EDS1–SAG101–NRG1A$^{\Delta N57}$ complexes, we assayed negative-stained samples using EM. EM images showed different oligomers of the complex, with a very small fraction appearing to be pentamer-like particles (Extended Data Fig. 2). This is consistent with SDS–polyacrylamide gel electrophoresis (SDS–PAGE) analysis of gel filtration fractions of the protein complex, showing that EDS1, SAG101 and NRG1A$^{\Delta N57}$ co-eluted at positions of different molecular weight. The negative staining data were further validated by two-dimensional averages of cryo-EM images of the samples, which showed dimeric, trimeric and tetrameric EDS1–SAG101–NRG1A$^{\Delta N57}$ (Fig. 1c and Extended Data Fig. 2). Some two-dimensional averages appeared to be pentameric, but one protomer had unclear density. Analysis of samples from gel filtration fractions eluted at molecular weight positions higher than that of the predicted pentameric complex produced similar results. We speculate that the N-terminal deletion of NRG1A compromises the oligomerization activity of the EDS1–SAG101–NRG1A$^{\Delta N57}$ complex. It is also possible that the pentameric complex dissociated during cryo-EM sample preparation, as observed for many protein complexes[36]. Due to preferential orientations of the particles of these intermediate oligomeric EDS1–SAG101–NRG1A$^{\Delta N57}$ complexes, we were not successful in obtaining three-dimensional reconstructions of them.

Activation of NRG1A by EDS1–SAG101

NRG1C probably associates with EDS1–SAG101 to antagonize NRG1A/B-mediated immune signalling[29]. We reasoned that the C-terminal WHD-LRR segment of NRG1A or NRG1B may similarly mediate interaction of these two hNLRs with EDS1–SAG101. We therefore co-expressed EDS1–SAG101 and an NRG1A variant (residues 391–809, termed NRG1A$^{WHD\text{-}LRR}$) together with the RPP1 resistosome in insect cells. As anticipated, pull-down assays showed that NRG1A$^{WHD\text{-}LRR}$ formed a stable complex with EDS1–SAG101 (Extended Data Fig. 3a). As observed with the formation of the EDS1–SAG101–NRG1A$^{\Delta N57}$ complex, assembly of EDS1–SAG101–NRG1A$^{WHD\text{-}LRR}$ was dependent on the RPP1 resistosome (Extended Data Fig. 3a). These results suggest that RPP1 resistosome-catalysed second messengers ADPr-ATP and /di-ADPR are also required for association of the EDS1–SAG101 dimer with NRG1A$^{WHD\text{-}LRR}$.

To demonstrate the structural mechanism of EDS1–SAG101 interaction with NRG1A$^{WHD\text{-}LRR}$, we solved a cryo-EM structure of the EDS1–SAG101–NRG1A$^{WHD\text{-}LRR}$ trimeric complex at a resolution of 3.1 Å (Fig. 2a, Extended Data Fig. 3 and Extended Data Table 1). The structure of EDS1–SAG101 in the ternary complex is nearly identical to that of ADPr-ATP-bound EDS1–SAG101 (Extended Data Fig. 4a), indicating that NRG1A$^{WHD\text{-}LRR}$ binding does not alter the conformation of EDS1–SAG101 bound by a TIR-catalysed small molecule. A well-defined ADPr-ATP molecule was found to bind between the EP domains of EDS1 and SAG101 (Extended Data Fig. 4b), which explains the RPP1 resistosome-dependent assembly of the EDS1–SAG101–NRG1A$^{WHD\text{-}LRR}$ complex. The structure shows that NRG1A$^{WHD\text{-}LRR}$ interaction with EDS1–SAG101 is mainly mediated by contacts of the LRR domain with the C-terminal EP domains of EDS1 and SAG101 (Fig. 2b). In addition, interaction is also established between NRG1A^{WHD} and EDS1–SAG101 but is much less dense than that mediated by the LRR domain. Binding of NRG1A$^{WHD\text{-}LRR}$ to EDS1 and SAG101 buries a surface area of 243 and 1,021 Å^2, respectively. The predominant contacts of NRG1A with SAG101, and variation at this surface in PAD4 (Extended Data Fig. 5a), would explain how NRG1A distinguishes EDS1–SAG101 from an EDS1–PAD4 dimer. Consistent with this, the NRG1A-interacting residues are variable in ADR1s (Extended Data Fig. 5b).

We previously proposed that ADPr-ATP-induced conformational changes in the C-terminal EP domain of SAG101 are required for EDS1–SAG101 interaction with NRG1A/B[4]. Like that of the ADPr-ATP-bound EDS1–SAG101 complex, the EP domain of SAG101 in EDS1–SAG101–NRG1A$^{WHD\text{-}LRR}$ rotates counterclockwise by around 15° compared with the apo-EDS1–SAG101 complex (Fig. 2b). Structural alignment between apo-EDS1–SAG101 and NRG1A$^{WHD\text{-}LRR}$-bound EDS1–SAG101 indicates that the NRG1A$^{WHD\text{-}LRR}$-binding surface of the C-terminal SAG101 EP domain is not discernible in apo-EDS1–SAG101 (Fig. 2b). Taken together, these structural data support the notion that ADPr-ATP binding induces conformational changes in the EP domain of SAG101 that are recognized by NRG1A, thus showing the mechanism of ADPr-ATP-induced EDS1–SAG101 recognition by NRG1A.

Structural studies suggest that binding of pathogen effectors triggers conformational changes in the NBD of sNLRs, allowing for exchange of ADP for ATP and allosteric activation of sNLRs[12]. In comparison, EDS1 and SAG101 are *Arabidopsis* host proteins that activate NRG1A/B[18,21,33]. Like pathogen effectors that are directly recognized by plant sNLRs[12], the ADPr-ATP-bound EDS1–SAG101 complex interacts with a C-terminal ascending lateral surface of NRG1A^{LRR} comprising loops connecting the β-strand to the convex surface (Fig. 2b). This suggests that modified host EDS1–SAG101 and pathogen effectors can use a conserved mechanism for the activation of NLRs. To examine this possibility, we superimposed the cryo-EM structure of inactive ZAR1$^{NOD\text{-}LRR}$ onto an AlphaFold2-predicted structure of inactive NRG1A with the N-terminal CC domain deleted (NRG1A$^{200-809}$, termed NRG1A$^{NOD\text{-}LRR}$). The superimposition shows that the structure of ZAR1$^{NOD\text{-}LRR}$ closely resembles that of NRG1A$^{NOD\text{-}LRR}$ (Extended Data Fig. 6a). The AlphaFold2-predicted structure of inactive NRG1A also has a high degree of conservation with NRG1A$^{WHD\text{-}LRR}$ in the cryo-EM structure of EDS1–SAG101–NRG1A$^{WHD\text{-}LRR}$ (Extended Data Fig. 6b). Combined analyses suggest that the inactive NRG1A$^{NOD\text{-}LRR}$ structure is a high-confidence prediction. Like effector protein interactions with inactive NLRs[14,15], ADPr-ATP-bound EDS1–SAG101 clashes with the NBD when it binds to the inactive NRG1A$^{NOD\text{-}LRR}$ (Fig. 2c). This would be expected to trigger conformational changes in the NBD and consequent exchange of ADP for ATP to activate the hNLR. Taken together, these results support the idea that allosterically induced conformational changes in the NBD represent a conserved activation mechanism for plant NLRs.

Recognition of EDS1–SAG101 by NRG1A

Contacts between the EP domain of SAG101 and NRG1A^{LRR} dominate the interaction between EDS1–SAG101 and NRG1A$^{WHD\text{-}LRR}$ (Fig. 2a). Notably, the very C-terminal α-helix of NRG1A packs against the SAG101 C-terminal end of α8 and the N-terminal end of α10, forming a short, three-helix bundle structure (Fig. 3a). In addition to the SAG101 α-helix, the loop region N-terminal to the short α-helix of NRG1A$^{WHD\text{-}LRR}$ interacts with α13 from the C-terminal EP domain of EDS1. The side chain of the last C-terminal residue F809 of NRG1A inserts between SAG101 α8 and α10 to form extensive hydrophobic contacts with its neighbouring residues (Y310, K313, K334 and F336; Fig. 3b). NRG1A F809 further forms a π–π interaction with SAG101 R324. In addition, the C-terminal free carboxy group makes a pair of hydrogen bonds with SAG101 R324 and K334 (Fig. 3b). L803 and L806 at the same side of the NRG1A C-terminal helix bind to a hydrophobic cavity formed by Y306, W309, K313 and F336 of SAG101, and NRG1A L805 and M809 locate at the hydrophobic cavity formed by F336 and I338 of SAG101. NRG1A R429 at the WHD forms a hydrogen bond with E335 of SAG101 to further strengthen the NRG1A$^{WHD\text{-}LRR}$–SAG101 association. Notably, NRG1A L803 also interacts

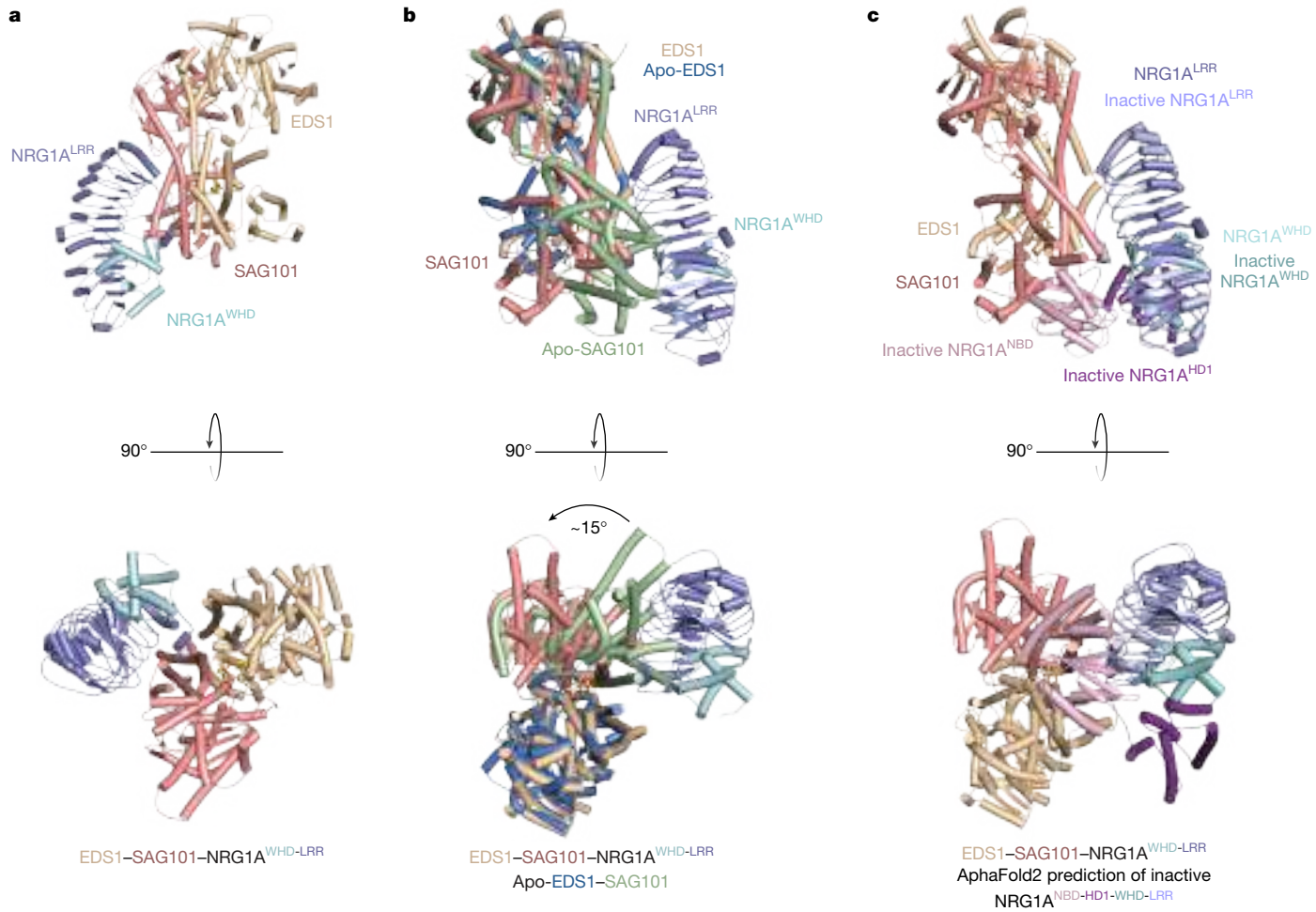

Fig. 2 | Induced conformational changes in EDS1–SAG101 are recognized by NRG1A$^{WHD\text{-}LRR}$. **a**, Two orientations of the overall structure of the EDS1–SAG101–NRG1A$^{WHD\text{-}LRR}$ complex shown in cartoon representation; ADPr-ATP is shown in stick form. **b**, The LRR domain mediates interaction of NRG1A$^{WHD\text{-}LRR}$ with the EP domain of SAG101. Structures of Apo-EDS1–SAG101 and EDS1–SAG101–NRG1A$^{WHD\text{-}LRR}$ were aligned with PyMOL. Colour codes for domains are indicated. The EP domain of SAG101 in EDS1–SAG101–NRG1A$^{WHD\text{-}LRR}$ (deep salmon) rotates by about 15° counterclockwise compared with that of SAG101 in apo-EDS1–SAG101 (green). **c**, EDS1–SAG101 clashes with the NBD when binding to NRG1A$^{WHD\text{-}LRR}$. Structural alignment between AlphaFold2-predicted inactive NRG1A, with its N-terminal CC domain truncated, and the cryo-EM structure of EDS1–SAG101–NRG1A$^{WHD\text{-}LRR}$. The NRG1A$^{WHD\text{-}LRR}$ segment in the cryo-EM structure was used as the template for alignment.

with EDS1 by packing against E416 and F419 (Fig. 3b). NRG1A$^{WHD\text{-}LRR}$–EDS1 interactions are further strengthened by van der Waals contacts of NRG1A N802 with EDS1 E416 and K420. Hydrophobic and van der Waals contacts largely mediate packing of the ascending lateral surface of the LRR domain (K606/M629/Y658) against the N-terminal end of SAG101 α10 and its preceding loop region (Fig. 3b). NRG1A Y660 is located at the centre of this interface. EDS1–SAG101 interacting residues are highly conserved in *Brassicaceae* (Extended Data Fig. 5c), suggesting a common mechanism for recognition of EDS1–SAG101 by NRG1s within this plant clade. In contrast, the last three hydrophobic residues of the very C-terminal α-helix of *At*NRG1A are substituted with polar amino acids in *Nicotiana benthamiana* (*Nb*) NRG1. This would explain why *At*EDS1–*At*SAG101 is unable to activate *Nb*NRG1 (ref. 23).

To verify the structural mechanism of EDS1–SAG101 recognition by NRG1A$^{WHD\text{-}LRR}$, we substituted key amino acids between NRG1A and EDS1–SAG101 and assessed the impact of these substitutions on their interaction in vitro. NRG1A$^{WHD\text{-}LRR}$ mutants with GST fused at the N terminus were individually co-expressed with EDS1, SAG101 and the RPP1 resistosome in insect cells, followed by GST-affinity purification. In support of the cryo-EM structure, deletion of the short NRG1A C-terminal α-helix (termed −LLQMF) resulted in a complete loss of NRG1A$^{WHD\text{-}LRR}$ interaction with EDS1–SAG101 (Fig. 3c and Extended Data Fig. 1b). Similar losses of interaction were observed with simultaneous mutations of three residues from this α-helix (L805A/M808A/F809A, denoted LMF, and H801A/L803A/L806A, denoted HLL) (Fig. 3c). Mutation of three residues (K606A/M629A/Y658A, denoted KMY) also abrogated NRG1A$^{WHD\text{-}LRR}$ interaction with EDS1–SAG101 (Fig. 3c). Reciprocally, mutations of three SAG101 residues (E335R/F336E/I338E, denoted EFI/REE) at this interface had a similar negative effect on the NRG1A$^{WHD\text{-}LRR}$–EDS1–SAG101 interaction (Fig. 3c). By contrast, substitutions of three SAG101 residues (H343R/E347R/R350E, denoted HER/RRE) outside the interface did not affect interaction with NRG1A$^{WHD\text{-}LRR}$ (Fig. 3c). Taken together, these results show that interactions mediated by the SAG101 short C-terminal α-helix and NRG1A LRR domain are necessary for NRG1A$^{WHD\text{-}LRR}$ association with ADPr-ATP activated EDS1–SAG101.

We next investigated whether the identified critical amino acids at the interface between EDS1–SAG101 and NRG1A$^{WHD\text{-}LRR}$ are important for EDS1–SAG101 signalling in plants. To this end, we reconstituted *At*NRG1A activation by transient co-expression of the TIR domain of *Arabidopsis* RPS4 (RPS4-TIR), *At*EDS1, *At*SAG101 (wild type or mutant) and *At*NRG1A (wild type or mutant) in a *Nb* mutant lacking *Nb*EDS1 and its paralogues *Nb*PAD4 and *Nb*SAG101a/b (*eds1 pad4 sag101a sag101b*, *Nb-epss*)[21,23]. *Agrobacteria*-infiltrated leaf zones were used

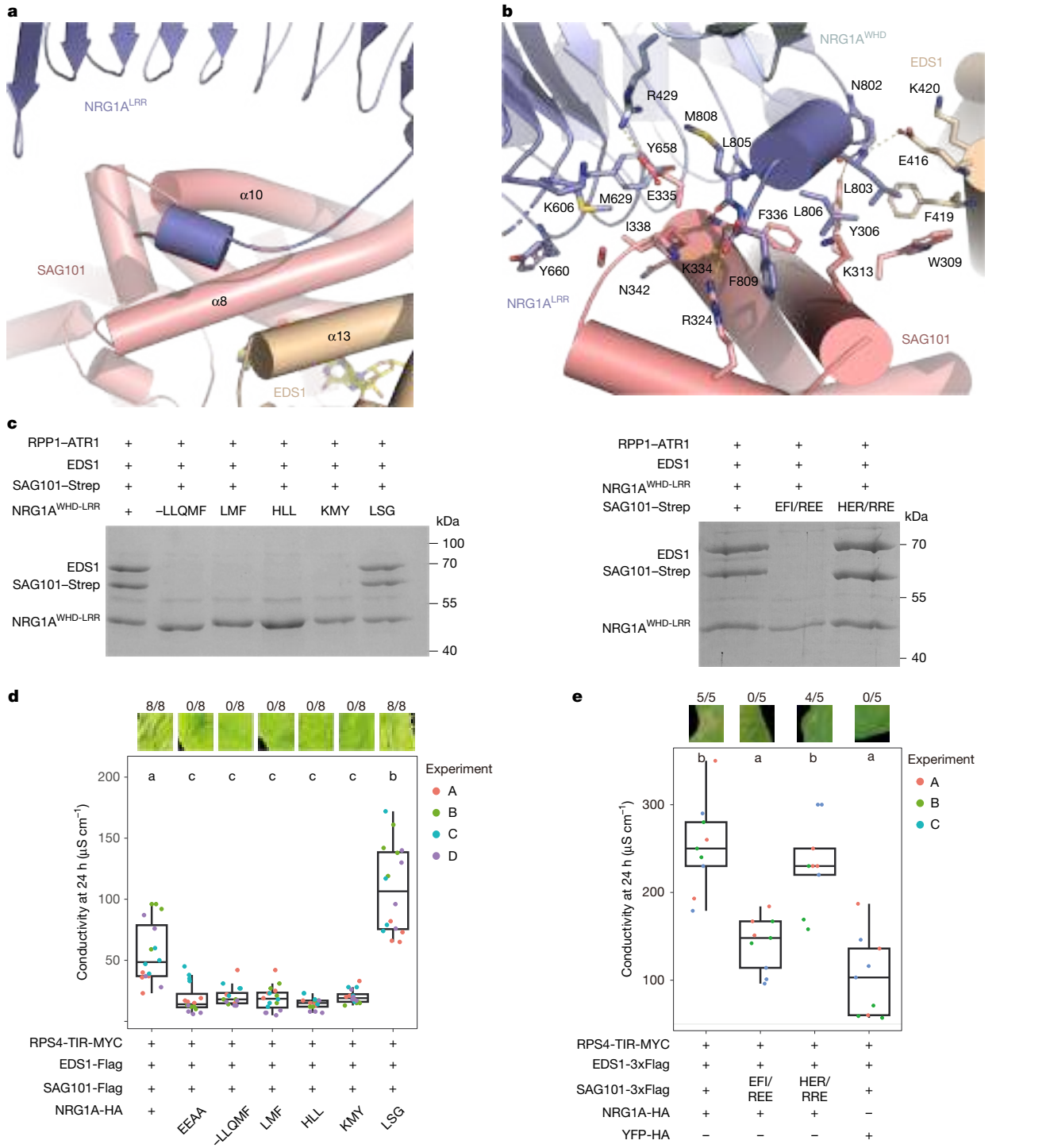

Fig. 3 | The LRR domain mediates NRG1A$^{WHD-LRR}$ interaction with the EP domains of EDS1–SAG101. a, A close-up view of the interaction between NRG1A$^{WHD-LRR}$ and EDS1–SAG101. **b**, Detailed interactions of NRG1A$^{WHD-LRR}$ with the EP domains of SAG101 and EDS1. Dashed lines represent polar interactions. **c**, Mutagenesis analysis of the interface between EDS1–SAG101 and NRG1A$^{WHD-LRR}$. NRG1A$^{WHD-LRR}$ wild-type (WT)/variants (–LLQMF (deletion of the C-terminal α-helix), LMF (L805A/M808A/F809A), HLL (H801A/L803A/L806A), KMY (K606A/M629A/Y658A) and LSG (L732F/S756Y/G757R)) indicated (left) were individually co-expressed with EDS1, SAG101 WT/variants (EFI/REE (E335R/F336E/I338E), HER/RRE (H343R/E347R/R350E)), RPP1 and ATR1 in insect cells. GST beads were used to purify proteins. Following removal of the GST tag, purified proteins were analysed by SDS–PAGE. The experiment was repeated three times with similar results. **d**, In planta cell death phenotypes and ion leakage measurement of *NRG1A* variants. *RPS4-TIR*, *EDS1*, *SAG101* and *NRG1A*_WT/variants (*EEAA* (*E14A*/*E27A*), *–LLQMF*, *LMF*, *HLL*, *KMY* and *LSG*) driven by the 35S promoter were co-expressed in *N. benthamiana epss* (*eds1 pad4 sag101a sag101b*). Cell death images were taken at 40 h; $n = 16$ images from four independent experiments (ABCD) were used as biological replicates for ion leakage measurement at 24 h. **e**, In planta cell death phenotypes and ion leakage measurement of SAG101 variants. *RPS4-TIR*, *EDS1*, *NRG1A* and *SAG101*_WT/variants (*EFI*/*REE* and *HER*/*RRE*), driven by the 35S promoter, were co-expressed in *Nb_epss*. Cell death images were taken at 48 h; $n = 9$ images from three independent biological replicates (ABC) were used for ion leakage measurement at 24 h. **d**,**e**, Numbers above images indicate ratios of cell death leaves/all inoculated leaves. Letters above boxplots indicate significant difference (one-way analysis of variance + Tukey's honest significant difference test ($P < 0.001$). Boxplots: minima, first quartile; maxima, third quartile; centre, median; whiskers extend to minimum and maximum values. Uncropped gels are shown in Supplementary Fig. 1.

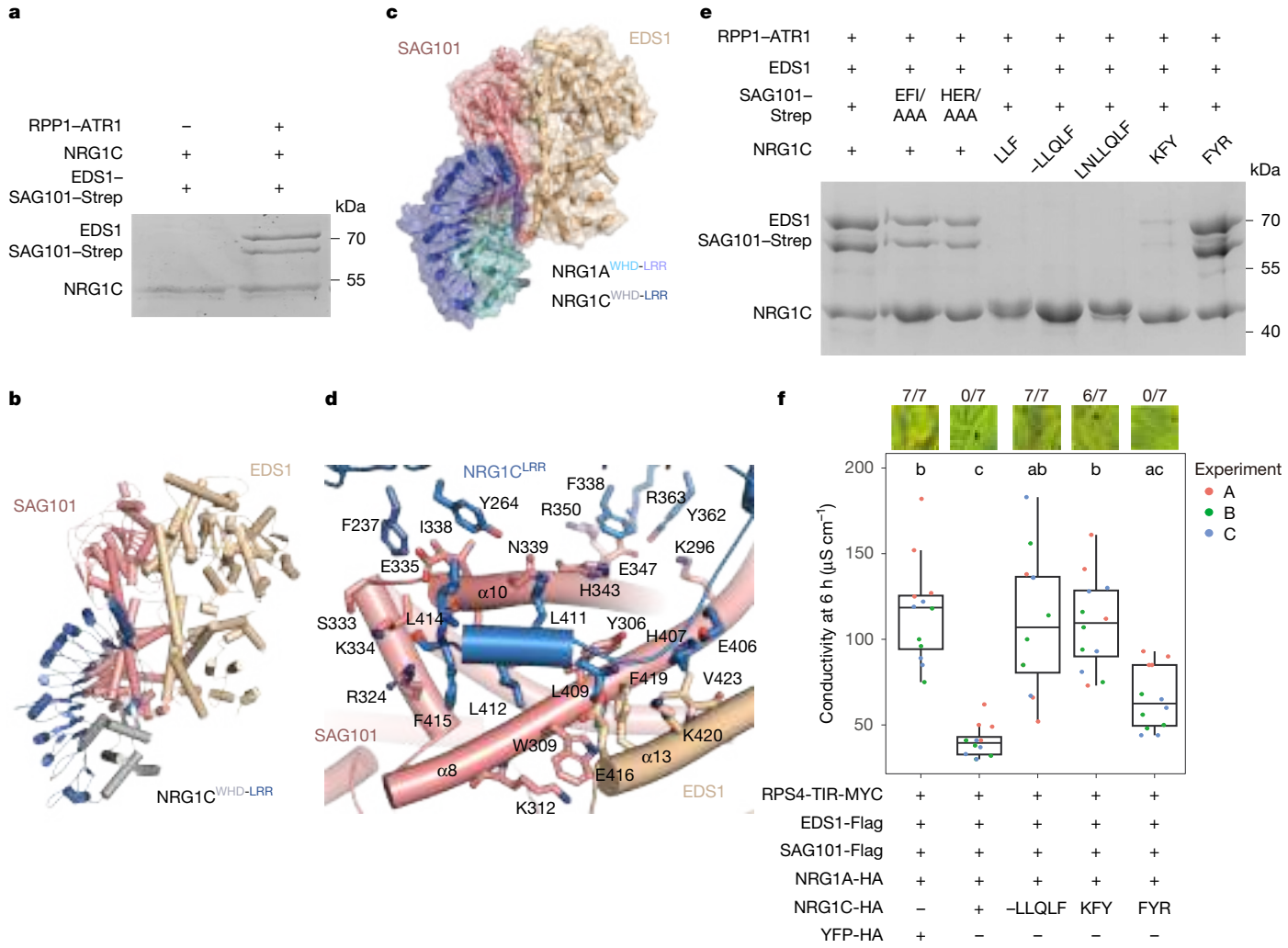

Fig. 4 | Crystal structure of EDS1–SAG101–NRG1C. a, EDS1–SAG101 interaction with NRG1C is RPP1 resistosome dependent. NRG1C was co-expressed with EDS1, SAG101, RPP1 and ATR1 in insect cells. The protein complex was purified and analysed as described in Fig. 3c. **b**, Overall crystal structure of the EDS1–SAG101–NRG1C complex shown in cartoon representation. **c**, Structural comparison of EDS1–SAG101–NRG1A$^{WHD\text{-}LRR}$ and EDS1–SAG101–NRG1C. The cryo-EM structure of EDS1–SAG101–NRG1A$^{WHD\text{-}LRR}$ and the crystal structure of EDS1–SAG101–NRG1C were aligned with PyMOL. EDS1–SAG101–NRG1A$^{WHD\text{-}LRR}$ is shown in surface form, and EDS1–SAG101–NRG1C in cartoon. **d**, Detailed interactions of NRG1C with the EP domains of EDS1–SAG101. Dashed lines represent polar interactions. **e**, Mutagenesis analysis of the interface between EDS1–SAG101 and NRG1C. NRG1C WT/ variants (LLF (L411A/L414A/F415A), –LLQLF (deletion of the short C-terminal α-helix), LNLLQLF (L409A/L411A/L412A/F415A), KFY (K214A/F237A/Y264A) and FYR (F338A/Y362A/R363A)) were individually co-expressed with EDS1, SAG101, RPP1 and ATR1 in insect cells. SAG101 WT/variants (EFI/AAA (E335A/F336A/I338A) and HER/AAA (H343A/E347A/R350A)) were individually co-expressed with EDS1, NRG1C, RPP1 and ATR1. Assays were performed as described in Fig. 3c. **a**,**d**, Experiments were independently repeated three times with similar results. **f**, In planta cell death phenotypes and ion leakage measurement of *NRG1C* WT/variants. *RPS4-TIR*, *EDS1*, *NRG1A*, *SAG101* and *NRG1C*_WT/variants (*–LLQLF*, *KFY* and *FYR*) driven by the 35S promoter were co-expressed in *Nb_epss*. Cell death images taken at 48 h are shown above each box. Numbers indicate ratios of leaves showing cell death/all inoculated leaves; $n = 12$ images from three experiments (ABC) were used as biological replicates for ion leakage measurement at 6 h. Different letters above boxplots denote significant difference (one-way analysis of variance + Tukey's honest significant difference test ($P < 0.001$)). Boxplots: minima, first quartile; maxima, third quartile; centre, median; whiskers extend to minimum and maximum values. For gel source data, see Supplementary Fig. 1.

for protein co-expression, followed by ion leakage assays to quantify cell death[23]. As anticipated, co-expression of wild-type NRG1A, EDS1 and SAG101 with RPS4-TIR induced cell death in *Nb-epss* leaves (Fig. 3d,e). By contrast, RPS4-TIR-induced cell death response was suppressed in *Nb-epss* expressing NRG1A mutants that had lost interaction with EDS1–SAG101 in vitro (Fig. 3d). SAG101 EFI/REE mutations that disrupted EDS1–SAG101 interaction with NRG1A also reduced RPS4-TIR-induced cell death (Fig. 3e). SAG101 HER/RRE mutations, however, had little effect on NRG1A-elicited cell death (Fig. 3e). Immunoblot analysis of wild-type and variant proteins expressed in *Nb-epss* leaves indicated that the mutations had not altered accumulation of NRG1A or SAG101 (Extended Data Fig. 1c,d). Collectively, these data suggest that the interaction surfaces between EDS1–SAG101 and NRG1A identified in the cryo-EM structure are functionally important for TNL-triggered cell death.

Structure of EDS1–SAG101–NRG1C

Co-immunoprecipitation data suggested that NRG1C associates with EDS1–SAG101 (ref. 29). Indeed, a structure-based sequence alignment showed that the amino acids mediating NRG1A$^{WHD\text{-}LRR}$ interaction with EDS1–SAG101 are conserved in NRG1C (Extended Data Fig. 5b). To test EDS1–SAG101–NRG1C interaction, we co-expressed the three proteins in insect cells and used a GST-NRG1C pulldown assay to detect complex formation. This affinity purification indicated no interaction of N-terminally GST-tagged NRG1C with EDS1–SAG101 (Fig. 4a

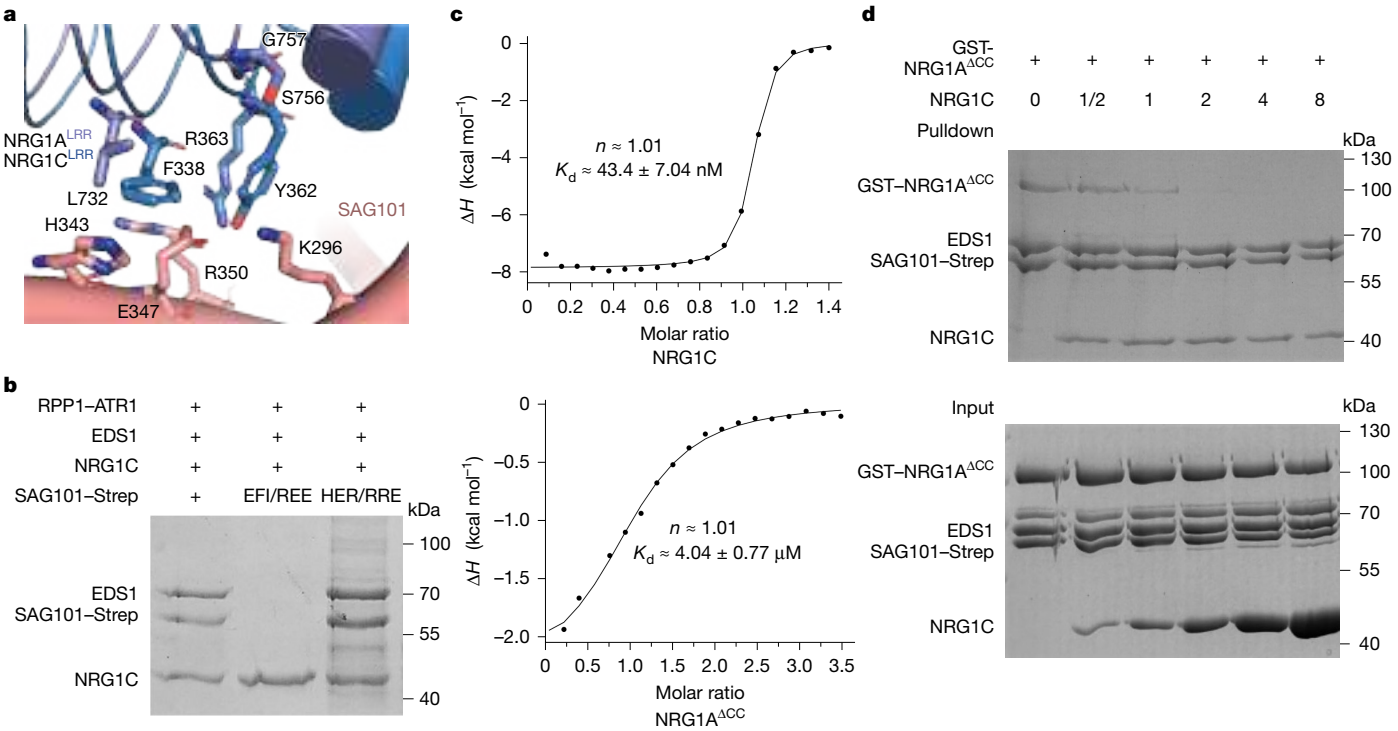

Fig. 5 | NRG1C outcompetes NRG1A$^{\Delta CC}$ for binding to EDS1–SAG101. a, Detailed interactions of the bulkier residues of NRG1C with the EP domain of SAG101. The EP, NRG1A and NRG1C LRR domains are shown in deep salmon, light blue and blue, respectively; the labelled bulkier residues of NRG1C LRR and their equivalents are shown in stick form; the residues of SAG101 interacting with these NRG1C bulkier amino acids are shown. **b**, Mutagenesis analysis of the interface between EDS1–SAG101 and NRG1C interaction. SAG101 WT/variants (EFI/REE (E335R/F336E/I338E) and HER/REE (H343R/E347R/R350E)) were individually co-expressed with EDS1, NRG1C, RPP1 and ATR1 in insect cells. Assays were performed as described in Fig. 3c. **c**, Quantification of the binding affinity of ADRr-ATP-bound EDS1–SAG101 with NRG1C (top) and NRG1A$^{\Delta CC}$ (bottom) by ITC; concentrations were 0.02 and 0.20 mM, respectively. Assays were performed in buffer containing 25 mM Tris-HCl pH 8.0, 150 mM NaCl and 3 mM DTT. **d**, Competitive assays for ADRr-ATP-bound EDS1–SAG101 interaction with NRG1A$^{\Delta CC}$ in the presence of different concentrations of NRG1C. ADRr-ATP-bound EDS1–SAG101 (with Strep-tag, 0.08 μmol) was incubated with 0.08 μmol of NRG1A$^{\Delta CC}$ (with GST tag) and varying amounts of NRG1C (0, 0.04, 0.08, 0.16, 0.32 and 0.64 μmol). The mixture was flowed through Strep beads; following extensive washing, the beads were analysed by SDS–PAGE and Coomassie brilliant blue staining. Experiments were independently repeated three times with similar results. For gel source data, see Supplementary Fig. 1.

and Extended Data Fig. 1e). We reasoned that NRG1C interaction with EDS1–SAG101 might require activation by an upstream TNL, similar to RPP1 resistosome-induced NRG1A interaction with EDS1–SAG101. We therefore added the RPP1 resistosome to the insect cell co-expression system. In this assay, NRG1C interacted strongly with EDS1–SAG101 (Fig. 4a), indicating that formation of the EDS1–SAG101–NRG1C complex is dependent on RPP1 resistosome-catalysed products.

To investigate the structural mechanism of NRG1C inhibition of EDS1 signalling, we purified and crystallized the EDS1–SAG101–NRG1C complex protein and solved its crystal structure with molecular replacement at a resolution of 2.5 Å (Fig. 4b, Extended Data Fig. 7a and Extended Data Table 2). As clearly defined by electron density, an ADPr-ATP molecule binds between the EP domains of EDS1 and SAG101 (Extended Data Fig. 4c). This structural observation supports the RPP1 resistosome-dependent NRG1C interaction with EDS1–SAG101. Structural alignment showed that EDS1–SAG101–NRG1C and EDS1–SAG101–NRG1A$^{WHD\text{-}LRR}$ are nearly identical (Fig. 4c). This observation indicates a shared mechanism of NRG1C and NRG1A interaction with ADPr-ATP-bound EDS1–SAG101; it also explains NRG1C-specific inhibition of NRG1A/B signalling in *Arabidopsis*[29].

As observed for the EDS1–SAG101–NRG1A$^{WHD\text{-}LRR}$ complex, the short C-terminal α-helix of NRG1C binds to the surface groove formed by α8 and α10 of SAG101 and α13 of EDS1 in the EDS1–SAG101–NRG1C crystal structure (Fig. 4d). In support of this structural observation, deletion of the C-terminal five residues or simultaneous mutation of hydrophobic residues in the short α-helix abolished NRG1C interaction with EDS1–SAG101 (Fig. 4e and Extended Data Fig. 1f). Furthermore, the deletion mutation resulted in a loss of NRG1C-inhibited NRG1A-dependent cell death triggered by RPS4-TIR in *Nb-epss* mutant plants (Fig. 4f and Extended Data Fig. 1g). Similar loss of NRG1C inhibition was observed with mutation of the three NRG1C amino acids (K214A/F237A/Y264A, denoted as KFY) that pack against α10 of SAG101 (Fig. 4f).

Competition between NRG1A and NRG1C

Despite marked structural similarity between EDS1–SAG101–NRG1C and EDS1–SAG101–NRG1A$^{WHD\text{-}LRR}$, several small residues of NRG1A (L732, S756, G757) at the interface with SAG101 are substituted with bulkier amino acids in NRG1C (F338, Y362 and R363; Extended Data Fig. 5b). These substitutions result in additional NRG1C contacts with SAG101 in the crystal structure of EDS1–SAG101–NRG1C (Fig. 5a). NRG1C binding to EDS1–SAG101 buries a surface area of 1,441 Å^2 compared with 1,264 Å^2 buried by binding of NRG1A$^{WHD\text{-}LRR}$ to EDS1–SAG101. The NRG1C FYR mutation (F338A/Y362A/R363A) did not disable its interaction with EDS1–SAG101 (Fig. 4e), consistent with NRG1C-SAG101 association being maintained by the interface that is shared with the NRG1A$^{WHD\text{-}LRR}$–EDS1–SAG101 complex (Fig. 3b). Similarly, mutation of SAG101 residues H343/E347/R350 that interact with F338/Y362/R363 of NRG1C did not impair EDS1–SAG101–NRG1C association (Fig. 5b). However, the NRG1C FYR mutation was less effective in inhibition of RPS4-TIR triggered, NRG1A-mediated cell death in *Nb-epss* leaves (Fig. 4f). Reciprocal substitutions (L732F/S756Y/G757R, denoted as LSG) of the three small NRG1A residues (L732, S756 and G757) by their equivalents in NRG1C (F338, Y362 and R363, respectively) did not obviously change the association

of NRG1A$^{WHD\text{-}LRR}$ with EDS1–SAG101 in vitro (Fig. 3c). By contrast, the NRG1A LSG mutation produced stronger RPS4-TIR-triggered ion leakage in *Nb-epss* leaves, suggesting that imposing the additional NRG1C interface on NRG1A enhances NRG1A signalling in vivo (Fig. 3d).

The above data suggest that NRG1C has a higher affinity for EDS1–SAG101 than NRG1A. To test this, we used isothermal titration calorimetry (ITC) to quantify the binding affinities of RPP1 resistosome-activated EDS1–SAG101 with NRG1C or NRG1A. The ITC results indicated that NRG1C binds to EDS1–SAG101 with a dissociation constant (K_d) of around 43 nM (Fig. 5c). Because NRG1A$^{WHD\text{-}LRR}$ protein alone could not be successfully purified, we used another NRG1A construct (residues 160–809, referred to as NRG1A$^{\Delta CC}$), which was successfully expressed and purified for ITC (Extended Data Fig. 7b). The ITC data showed that NRG1A$^{\Delta CC}$ protein exhibited a much weaker EDS1–SAG101-binding affinity, with a K_d of about 4 μM, nearly 100-fold lower than that of NRG1C with EDS1–SAG101 (Fig. 5c).

The stronger EDS1–SAG101-binding affinity of NRG1C suggests that this truncated NLR protein would efficiently outcompete NRG1A for binding to EDS1–SAG101. To test this prediction, we first purified EDS1–SAG101 previously co-expressed with the RPP1 resistosome in insect cells to produce EDS1–SAG101 bound by ADPr-ADP or di-ADPR[4]. The purified EDS1–SAG101 protein was then incubated with NRG1A$^{\Delta CC}$, together with varying amounts of NRG1C. Affinity purification was used to determine the amount of NRG1A bound to EDS1–SAG101. As shown in Fig. 5d, NRG1A$^{\Delta CC}$ was efficiently pulled down by EDS1–SAG101 in the absence of NRG1C. With increasing amounts of NRG1C protein, the amount of NRG1A$^{\Delta CC}$ bound to EDS1–SAG101 gradually reduced. At a ratio of 2:1 NRG1C:NRG1A$^{\Delta CC}$, almost no NRG1A$^{\Delta CC}$ was detected in association with EDS1–SAG101, indicating that all NRG1A$^{\Delta CC}$ had been outcompeted by NRG1C (Fig. 5d). We found that NRG1C was much less efficient in outcompeting NRG1A$^{WHD\text{-}LRR}$ in the preformed EDS1–SAG101- NRG1A$^{WHD\text{-}LRR}$ complex (Extended Data Fig. 7c). As discussed above, the NBD in inactive NRG1A is positioned to clash with activated EDS1–SAG101 (Extended Data Fig. 7d). This is predicted to trigger conformational changes in the NBD, but also to compromise the interaction between EDS1–SAG101 and the LRR domain of NRG1A, due to partial blocking of EDS1–SAG101 binding sites. This feature would further contribute to a higher EDS1–SAG101 binding affinity of NRG1C than NRG1A. Taken together, these results suggest that NRG1C functions to sequester the activated EDS1–SAG101 from inactive NRG1A.

Discussion

Arabidopsis hNLRs NRG1 and ADR1 form resistosomes in response to pathogen invasion, but the mechanism underlying their activation remains less well understood. In contrast to sNLRs, which are directly activated by pathogen effectors or host proteins that are modified by effectors, NRG1 and ADR1 are activated by the host EDS1 family members[4,19]. Our current study shows that EDS1–SAG101 interacts with the C-terminal ascending lateral surface of NRG1A^{LRR}, a region known for recognizing pathogen effectors in several sNLRs[12]. These observations suggest that EDS1–SAG101 and pathogen effectors might activate sNLRs and hNLRs by a conserved structural mechanism. Unlike pathogen effectors, the NRG1A-binding activity of EDS1–SAG101 requires triggering by a catalytic product of RPP1 or other TNL resistosomes. Structural predictions indicate that EDS1–SAG101 binding allosterically induces conformational changes in NRG1A^{NBD} to promote NRG1A oligomerization (Fig. 2c). This mechanism was previously demonstrated for the activation of sNLRs, including TNLs and CNLs[2,13,14].

EDS1–SAG101 binding induces NRG1A oligomerization (Fig. 1b,c). Notably, NRG1A oligomers contain between two and four, rather than the predicted five or six, EDS1–SAG101–NRG1A protomers in vitro (Fig. 1c). This might reflect a requirement for additional components to mediate complete assembly of the NRG1 resistosome in vivo. This possibility aligns with a previous finding that signalling from cell surface receptors promotes the formation of the NRG1 resistosome[18] in vivo. In our analysis, EDS1–SAG101 remains associated with NRG1A following its activation (Fig. 1b,c). This is consistent with the earlier study showing that the NRG1 resistosome contains EDS1–SAG101[18], but differs from another study that did not detect EDS1 or SAG101 as part of the NRG1A resistosome[35]. This discrepancy could have resulted from variation in the conditions used to detect interactions between NRG1A and EDS1–SAG101. Regardless of the precise reason for the unsuccessful reconstitution of the NRG1 resistosome, our findings suggest that plant host immunity components EDS1–SAG101 and pathogen effectors adopt a conserved structural mechanism for activation of NLRs.

The EDS1–SAG101 complex is not directly involved in detection of pathogens, but senses pathogen disturbance by recognizing pathogen effector-induced, TIR-catalysed second messengers ADPr-ATP/di-ADPR, and therefore serves as a signalling convergence point for multiple TNLs and TIR enzymes to stimulate immunity and host cell death in dicot plants[34]. ADPr-ATP/di-ADPR-induced conformational changes in the SAG101 EP domain create 'modified self' that is recognized by NRG1A and NRG1B, thus acting as a molecular signature for pathogen attack and, potentially, other stresses[37]. pRib-ADP/AMP binding to EDS1–PAD4 similarly induces conformational changes in the EP domain of PAD4 (ref. 19), suggesting that a similar mechanism exists for ADR1 activation by EDS1–PAD4 dimers to potentiate TIR-catalysed immunity.

Conceptually, NRG1A activation by EDS1–SAG101 does not conform to the guard model, in which guardee proteins are direct targets for pathogen effectors and their effector modifications are sensed by NLRs[8,38]. Our data show that a modified self by non-pathogen components can also activate NLRs. This aligns with a danger model in which plants sense endogenous danger signals to mount responses to diverse challenges[39]. In this model, the TNL resistosome- or TIR-catalysed second messengers act as danger signals that bind to and modify EDS1–SAG101, leading to the assembly of an NRG1A resistosome (Extended Data Fig. 8). It will be of interest to investigate whether other NLRs use a similar mechanism for activation, potentially to propagate defences beyond sites of pathogen effector detection.

In *Arabidopsis*, the EDS1–PAD4–ADR1 module potentiates TIR-catalysed defence triggered by pathogen-sensing cell surface and intracellular NLR receptors[27,28]. The importance of the EDS1–PAD4 pRib-AMP/ADP binding site, in regard to its role in PTI and ETI signalling[27,40,41], suggests that activation of ADR1 by modified EDS1–PAD4 mediates this process. Some plant NLRs regulate responses to abiotic stress[37,42,43], and an NLR was identified that prevents premature synergid cell death in reproductive development[44], further supporting functions of NLRs beyond recognition of pathogen effectors.

Our data show that specific inhibition of EDS1–SAG101 by NRG1C is achieved through the direct interaction of TIR-catalysed, small-molecule-activated EDS1–SAG101 with NRG1C. This finding makes sense of the observation that NRG1C homologues are not functionally interchangeable between in *N. benthamiana* and *Brassicaceae*[29]. A higher EDS1–SAG101 binding activity of NRG1C than NRG1A, and its induction in response to pathogen infection[29,41], suggest that NRG1C has the capacity to effectively outcompete NRG1A in binding the EDS1–SAG101 complex. This might explain the higher NRG1C interaction signal than that of NRG1A and NRG1B in EDS1–SAG101 immunoprecipitation analyses of pathogen-activated *Arabidopsis* leaves[21,29]. Because NRG1C inhibition of NRG1A activation by EDS1–SAG101 depends on a TIR small-molecule stimulus, it would provide a potentially crucial feedback mechanism to limit host hypersensitive cell death at pathogen infection sites.

The site within the cell in which NRG1C inhibits NRG1A activation has not been established. Constitutively active NRG1A predominantly localized to the plasma membrane[35], whereas nuclear and plasma membrane NRG1A pools were detected in TNL-triggered cells[18]. Given the strong induction of NRG1C by pathogen infection[29,41], we speculate that EDS1–SAG101–NRG1C co-accumulation in both compartments following

TNL activation would enable efficient sequestration of EDS1–SAG101 by NRG1C. Together, these data provide a molecular basis for NRG1C inhibition of NRG1A-mediated immune responses. We propose that the balance between NRG1A/B and NRG1C levels contributes to fine-tuning of EDS1–SAG101 immune output in plants.

Online content

Any methods, additional references, Nature Portfolio reporting summaries, source data, extended data, supplementary information, acknowledgements, peer review information; details of author contributions and competing interests; and statements of data and code availability are available at https://doi.org/10.1038/s41586-024-08521-7.

1. Jones, J. D. G. & Dangl, J. L. The plant immune system. *Nature* **444**, 323–329 (2006).
2. Ma, S. et al. Direct pathogen-induced assembly of an NLR immune receptor complex to form a holoenzyme. *Science* **370**, eabe3069 (2020).
3. Martin, R. et al. Structure of the activated ROQ1 resistosome directly recognizing the pathogen effector XopQ. *Mol. Plant Microbe Interact.* **34**, eabd9993 (2021).
4. Jia, A. et al. TIR-catalyzed ADP-ribosylation reactions produce signaling molecules for plant immunity. *Science* **377**, eabq8180 (2022).
5. Chisholm, S. T., Coaker, G., Day, B. & Staskawicz, B. J. Host-microbe interactions: shaping the evolution of the plant immune response. *Cell* **124**, 803–814 (2006).
6. Zhou, J. & Zhang, Y. Plant immunity: danger perception and signaling. *Cell* **181**, 978–989 (2020).
7. Cui, H., Tsuda, K. & Parker, J. E. Effector-triggered immunity: from pathogen perception to robust defense. *Annu. Rev. Plant Biol.* **66**, 487–511 (2015).
8. Dodds, P. N. & Rathjen, J. P. Plant immunity: towards an integrated view of plant-pathogen interactions. *Nat. Rev. Genet.* **11**, 539–548 (2010).
9. van der Biezen, E. A. & Jones, J. D. G. Plant disease-resistance proteins and the gene-for-gene concept. *Trends Biochem. Sci* **23**, 454–456 (1998).
10. Jubic, L. M., Saile, S., Furzer, O. J., El Kasmi, F. & Dangl, J. L. Help wanted: helper NLRs and plant immune responses. *Curr. Opin. Cell Biol.* **50**, 82–94 (2019).
11. Feehan, J. M., Castel, B., Bentham, A. R. & Jones, J. D. G. Plant NLRs get by with a little help from their friends. *Curr. Opin. Cell Biol.* **56**, 99–108 (2020).
12. Hu, Z. & Chai, J. Assembly and architecture of NLR resistosomes and inflammasomes. *Annu. Rev. Biophys.* **52**, 207–228 (2023).
13. Wang, J. et al. Reconstitution and structure of a plant NLR resistosome conferring immunity. *Science* **364**, eaav5870 (2019).
14. Förderer, A. et al. A wheat resistosome defines common principles of immune receptor channels. *Nature* **610**, 532–539 (2022).
15. Zhao, Y. et al. Pathogen effector AvrSr35 triggers Sr35 resistosome assembly via a direct recognition mechanism. *Sci. Adv.* **8**, eaav5870 (2022).
16. Liu, F. et al. Activation of the helper NRC4 immune receptor forms a hexameric resistosome. *Cell* **187**, 4877–4889 (2024).
17. Jacob, P. et al. Plant "helper" immune receptors are Ca^{2+}-permeable nonselective cation channels. *Science* **373**, 420–425 (2021).
18. Feehan, J. M. et al. Oligomerization of a plant helper NLR requires cell-surface and intracellular immune receptor activation. *Proc. Natl Acad. Sci. USA* **120**, e2210406120 (2023).
19. Huang, S. et al. Identification and receptor mechanism of TIR-catalyzed small molecules in plant immunity. *Science* **377**, eabq3297 (2022).
20. Dongus, J. A. & Parker, J. E. EDS1 signalling: at the nexus of intracellular and surface receptor immunity. *Curr. Opin. Cell Biol.* **62**, 102039 (2021).
21. Sun, X. et al. Pathogen effector recognition-dependent association of NRG1 with EDS1 and SAG101 in TNL receptor immunity. *Nat. Commun.* **12**, 3335 (2021).
22. Wu, Z., Tian, L., Liu, X., Zhang, Y. & Li, X. TIR signal promotes interactions between lipase-like proteins and ADR1-L1 receptor and ADR1-L1 oligomerization. *Plant Physiol.* **187**, 681–686 (2021).
23. Lapin, D. et al. A coevolved EDS1-SAG101-NRG1 module mediates cell death signaling by TIR-domain immune receptors. *Plant Cell* **31**, 2430–2455 (2019).
24. Castel, B. et al. Diverse NLR immune receptors activate defence via the RPW8-NLR NRG1. *New Phytol.* **222**, 966–980 (2019).
25. Saile, S. C. et al. Two unequally redundant "helper" immune receptor families mediate *Arabidopsis thaliana* intracellular "sensor" immune receptor functions. *PLoS Biol.* **18**, e3000783 (2020).
26. Wu, Z. S. et al. Differential regulation of TNL-mediated immune signaling by redundant helper CNLs. *New Phytol.* **222**, 938–953 (2019).
27. Pruitt, R. N. et al. The EDS1-PAD4-ADR1 node mediates *Arabidopsis* pattern-triggered immunity. *Nature* **598**, 495–499 (2021).
28. Tian, H. et al. Activation of TIR signalling boosts pattern-triggered immunity. *Nature* **598**, 500–503 (2021).
29. Wu, Z. et al. The N-terminally truncated helper NLR NRG1C antagonizes immunity mediated by its full-length neighbors NRG1A and NRG1B. *Plant Cell* **34**, 1621–1640 (2022).
30. Wang, J., Song, W. & Chai, J. Structure, biochemical function, and signaling mechanism of plant NLRs. *Mol. Plant* **16**, 75–95 (2023).
31. Ao, K. & Li, X. Indirect recognition of pathogen effectors by NLRs. *Essays Biochem.* **66**, 485–500 (2022).
32. Contreras, M. P. et al. The nucleotide binding domain of NRC-dependent disease resistance proteins is sufficient to activate downstream helper NLR oligomerization and immune signaling. *New Phytol.* **243**, 345–361 (2024).
33. Chai, J. J., Song, W. & Parker, J. E. New biochemical principles for NLR immunity in plants. *Mol. Plant Microbe Interact.* **36**, 468–475 (2023).
34. Locci, F. & Parker, J. E. Plant NLR immunity activation and execution: a biochemical perspective. *Open Biol.* **14**, 230387 (2024).
35. Wang, Z. et al. Plasma membrane association and resistosome formation of plant helper immune receptors. *Proc. Natl Acad. Sci. USA* **120**, e2222036120 (2023).
36. Danev, R., Yanagisawa, H. & Kikkawa, M. Cryo-electron microscopy methodology: current aspects and future directions. *Trends Biochem. Sci.* **44**, 837–848 (2019).
37. Ariga, H. et al. NLR locus-mediated trade-off between abiotic and biotic stress adaptation in *Arabidopsis*. *Nat. Plants* **3**, 17072 (2017).
38. Van der Hoorn, R. A., De Wit, P. J. & Joosten, M. H. Balancing selection favors guarding resistance proteins. *Trends Plant Sci.* **7**, 67–71 (2002).
39. Gust, A. A., Pruitt, R. & Nurnberger, T. Sensing danger: key to activating plant immunity. *Trends Plant Sci.* **22**, 779–791 (2017).
40. Bhandari, D. D. et al. An EDS1 heterodimer signalling surface enforces timely reprogramming of immunity genes in *Arabidopsis*. *Nat. Commun.* **10**, 772 (2019).
41. Dongus, J. A. et al. Cavity surface residues of PAD4 and SAG101 contribute to EDS1 dimer signaling specificity in plant immunity. *Plant J.* **110**, 1415–1432 (2022).
42. Chini, A., Grant, J. J., Seki, M., Shinozaki, K. & Loake, G. J. Drought tolerance established by enhanced expression of the CC-NBS-LRR gene, ADR1, requires salicylic acid, EDS1 and ABI1. *Plant J.* **38**, 810–822 (2004).
43. Zhu, Y., Qian, W. & Hua, J. Temperature modulates plant defense responses through NB-LRR proteins. *PLoS Pathog.* **6**, e1000844 (2010).
44. Volz, R., Harris, W., Hirt, H. & Lee, Y. H. ROS homeostasis mediated by MPK4 and SUMM2 determines synergid cell death. *Nat. Commun.* **13**, 1746 (2022).

Methods

Plasmid constructions

Plasmid constructions of non-tagged *EDS1* (residues 1–623), C-terminally twin-StrepII-tagged *SAG101* (residues 1–537), N-terminally GST-tagged *NRG1A* (residues 58–809, termed *NRG1A*$^{\Delta N57}$), C-terminally twin-StrepII-tagged *RPP1_WsB* (residues 61–1,221) and non-tagged *ATR1_Emoy2* (residues 52–311) used in this study are the same as those used in a previous study[4]. For the new *NRG1C* constructs, targeted constructs were PCR amplified from codon-optimized *NRG1C* recombinant vectors (GENEWIZ), and then homologously recombined into the N-terminally GST-tagged pFastbac 1 vector. N-terminally truncated forms of *NRG1A* (residues 160–809, termed *NRG1A*$^{\Delta CC}$, and residues 391–809, termed *NRG1A*$^{WHD\text{-}LRR}$) were generated using *NRG1A*$^{\Delta N57}$ as the template.

Coding sequences without stop codons of *NRG1A*, *NRG1C*, *SAG101* and *RPS4-TIR* were amplified and cloned into pENTR/D-TOPO (catalogue no. K240020, Thermo Fisher Scientific). Further site-directed mutagenesis of *NRG1A*, *SAG101* and *NRG1C* was performed using their entry clones as templates. All *NRG1A* and *NRG1C* variants were transferred from entry clones to destination vector pXCSG-3xHA-StrepII for *Agrobacterium*-mediated transient expression in *N. benthamiana*. *RPS4-TIR* was recombined into pXCSG-MYC destination vector. *SAG101* variants were recombined into pXCSG-3×Flag destination vector using LR Clonase II (catalogue no. 11791100, Life Technologies).

Recombinant protein expression and purification

The Bac-to-Bac baculovirus expression system (Invitrogen, catalogue no. 10359-016) was used to express recombinant proteins. For purification of the EDS1–SAG101–NRG1A complex, recombinant baculoviruses of RPP1, ATR1, EDS1, SAG101 and NRG1A$^{\Delta N57}$ were used to co-infect *Sf*21 insect cells (Thermo Fisher Scientific) at 28 °C. After 48 h of infection, cells were harvested and resuspended in resuspension buffer containing 25 mM Tris-HCl pH 8.0, 150 mM NaCl, 3 mM DTT, 1 mM ATP and 1 mM phenylmethanesulfonyl fluoride, and were then lysed by sonification and centrifuged at 13,000 rpm for 1 h at 4 °C for collection of supernatant. Glutathione Sepharose 4B beads (GE Healthcare) were used to purify the EDS1–SAG101–NRG1A$^{\Delta N57}$ complex protein from the supernatant. Following flowing of the supernatant twice through the column, three column volumes of resuspension buffer were used to wash the beads and the target protein was then eluted in buffer containing 25 mM Tris-HCl pH 8.0, 150 mM NaCl, 3 mM DTT and 15 mM glutathione. The protein was further purified by size-exclusion chromatography (Superdex 6 increase 10/300, GE Healthcare) in buffer containing 25 mM Tris-HCl pH 8.0, 150 mM NaCl and 3 mM DTT. A similar protocol was used for purification of complexes EDS1–SAG101–NRG1A$^{WHD\text{-}LRR}$ and EDS1–SAG101–NRG1C.

Crystallization, data collection, structure determination and refinement

Purified EDS1–SAG101–NRG1C protein was concentrated to about 5.8 mg ml^{-1}, and crystallization of the complex performed using hanging-drop vapour diffusion by mixing 1 µl of protein with 1 µl of reservoir solution at 18 °C. Diffraction-quality crystals of the EDS1–SAG101–NRG1C complex were obtained in buffer containing 5% v/v (±)-2-methyl-2,4-pentanediol, 0.1 M HEPES pH 7.5 and 10% w/v polyethylene glycol 10,000. All diffraction datasets were collected at Shanghai Synchrotron Radiation Facility. Data were processed using software packages CCP4i and HKL2000 (ref. 45). The crystal structure of EDS1–SAG101–NRG1C was determined by molecular replacement using EDS1–SAG101 (Protein Data Bank 7XJP) and an AlphaFold2-predicted structure of NRG1C as the search templates, with PHASER[46]. The molecular replacement model was built with Coot[47] and subsequently subjected to refinement by Phenix_real_space_refine. Statistics of diffraction data and refinement of the EDS1–SAG101–NRG1C model are summarized in Extended Data Table 2. Structural figures were prepared using PyMOL (http://www.pymol.org/).

ITC assay

EDS1–SAG101 was co-expressed with the RPP1 resistosome in insect cells and purified as described above. The binding affinities of EDS1–SAG101 with NRG1C or NRG1A$^{\Delta CC}$ were measured using MicroCal PEAQ-ITC at 25 °C in buffer containing 25 mM Tris-HCl pH 8.0, 150 mM NaCl and 3 mM DTT; 0.2 mM NRG1A$^{\Delta CC}$ or NRG1C was then injected (19 × 2.0 µl) at 150-s intervals into the stirred (750 rpm) sample cell (volume approximately 280 µl) containing 0.02 mM EDS1–SAG101. Curve fitting and calculation of the binding affinity of all titration data were analysed using MicroCal PEAQ-ITC Analysis Software.

GST pulldown assay

The GST pulldown assay was used to test EDS1–SAG101 interaction with wild-type or mutant NRG1A$^{WHD\text{-}LRR}$ or NRG1C. Wild-type or mutant N-terminally GST-tagged NRG1A$^{WHD\text{-}LRR}$ and NRG1C were co-expressed with RPP1, ATR1, EDS1 and SAG101 as described above. Complexes EDS1–SAG101–NRG1A$^{WHD\text{-}LRR}$ and EDS1–SAG101–NRG1C were purified using Glutathione Sepharose 4B beads. Following extensive washing, the GST tag of NRG1A/C was removed in buffer containing 25 mM Tris-HCl pH 8.0, 150 mM NaCl, 3 mM DTT and human rhinovirus 3C protease. Proteins were analysed with SDS–PAGE and Coomassie brilliant blue staining.

Competition experiments

N-terminally GST-tagged NRG1A$^{\Delta CC}$ (0.08 µmol, purified as described above) was mixed with purified non-tagged NRG1C; ratios between NRG1A$^{\Delta CC}$ and NRG1C in the mixture were 1:0, 1:0.5, 1:1, 1:2, 1:4 and 1:8. Mixtures were incubated for 30 min and then an equal molar amount of the purified EDS1–SAG101 protein, previously co-expressed with the RPP1 resistosome, was added. Mixtures were incubated on ice for a further 30 min, followed by Strep affinity purification. Strep beads were then washed, and bound proteins eluted and analysed using SDS–PAGE and Coomassie brilliant blue staining.

Cryo-EM sample preparation and data acquisition

For cryo-EM analysis, the purified EDS1–SAG101–NRG1A complex protein was concentrated to around 1 mg ml^{-1}. Following 2-min evacuation, Quantifoil Au R 1.2/1.3, 300-mesh holey carbon girds were glow discharged for 30 s at medium level in Harrick Plasma, and 3 µl of protein was applied to the grids. Grids were blotted by filter paper (Ted Pella, Inc.) for 2.5–3.5 s at 8 °C and 100% humidity, and then flash-frozen in liquid ethane using an FEI Vitrobot Mark IV.

Cryo-EM data were collected on a Thermo Scientific Krios G4 electron microscope operating at 300 kV and equipped with a Gatan Quantum energy filter and Gatan K3 direct-detection camera at ×105,000 magnification, with a physical pixel size of 0.425 Å. Micrographs were recorded using EPU 2.8.1.10 data collection software, with defocus values ranging from −1.0 to −2.0 µM, dose-fractionated into 40 frames at an exposure rate of 15 pixels per second and with a total accumulated dose of roughly 50 electrons per Å^2. A total of 6,930 stacks were collected.

Image processing and three-dimensional reconstruction

Stacks were 2× Fourier binned, aligned, dose weighted and summed using MotionCor2 (ref. 48), resulting in an individual pixel size of 0.85 Å. Contrast transfer function was corrected using CTFFIND4 (ref. 49), and poor-quality micrographs were removed manually. Further processing was performed using RELION 4.0 (refs. 50–52). The cryo-EM processing workflow for EDS1–SAG101–NRG1A$^{WHD\text{-}LRR}$ is summarized in Extended Data Fig. 3. A total of 5,978,183 particles were autopicked using Laplacian of Gaussian from 6,913 stacks in RELION 4.0. Several rounds of two-dimensional classification were performed, to remove contaminants and noise in the raw automatically picked particles. Following two-dimensional classification, the selected particles

were used to generate an ab initio map as the initial reference model. Two rounds of three-dimensional classification were then performed, and 275,262 good particles were selected for final three-dimensional autorefinement. Following contrast transfer function and post-processing, final resolution of the three-dimensional reconstruction was 3.09 Å, based on gold standard Fourier shell correction 0.143 criteria[53].

Model building and refinement

Reconstruction of EDS1–SAG101–NRG1A$^{WHD\text{-}LRR}$ EM density was used for initial model building. The crystal structure of EDS1–SAG101–NRG1C was docked into the EM density in Chimera to build the initial model of EDS1–SAG101–NRG1A$^{WHD\text{-}LRR}$ (ref. 54), which included an ADPr-ATP. Local differences and sequence assignment of NRG1A were manually adjusted in Coot[47]. Models were refined using multiple rounds of Phenix_real_space refine[55], validation was performed with MolProbity and EMRinger[55] and statistics are summarized in Extended Data Table 1.

Agrobacterium-mediated transient expression in *N. benthamiana*

Expression constructs (*p35S:EDS1-3xFLAG*, *p35S: SAG101-3xFLAG* and *p35S: NRG1A-3xHA*) were described previously[21]. All constructs used for transient expression in *N. benthamiana* were electroporated into *Rhizobium radiobacter* (*Agrobacterium tumefaciens*) GV3101 pMP90RK or pMP90. *A. tumefaciens* strains from master stocks were freshly streaked on yeast extract broth plates with the appropriate antibiotics and incubated for 24 h at 28 °C. Cells were collected from plates and resuspended in induction buffer (10 mM MES pH 5.32, 10 mM $MgCl_2$ and 150 nM acetosyringone) at optical density OD_{600} = 0.2. Strains carrying NRG1C or its variants were resuspended at OD_{600} = 0.6 to sufficiently inhibit cell death in the *N. benthamiana* reconstitution assay. Agrobacteria expressing gene-silencing suppressors p19 and CMV2b (OD_{600} = 0.1) were co-infiltrated with test Agrobacteria strains into leaves of 4–5-week-old *N. benthamiana*, using a 1-ml syringe through a shallow scratch created with a medical needle.

For the cell death assay, leaves were spot infiltrated and evaluated for macroscopic tissue collapse 2 days after infiltration. Plants were randomly infiltrated with different Agrobacteria strain combinations. Leaf discs with a diameter of 7 mm were punched from infiltrated regions for ion leakage measurement, as described previously[21]. The measurement was conducted in a blinded manner, where the individual measuring ion leakage was unaware of the combinations. Significant difference was tested by one-way analysis of variance with Tukey's honest significant difference test ($P < 0.001$). Two frozen leaf discs were crushed into fine powder at 30 Hz for 1 min, then 100 µl of 2× Laemmli buffer (125 mM Tris-HCl pH 6.8, 4% (v/v) SDS, 20% (v/v) glycerol, 200 mM DTT and 0.02% (w/v) bromophenol blue) were added to the crushed material and boiled at 95 °C for 5 min. Samples were centrifuged for 5 min at 12,000 rpm to obtain supernatants, which were loaded onto 7.5% SDS–PAGE gels. After running for 40 min at 200 V, proteins in the gels were transferred onto nitrocellulose membranes using a Trans-Blot Turbo (Bio-Rad). Antibodies used for immunoblotting were α-MYC (catalogue no. 71D10, Cell Signaling), α-HA (catalogue no. 11867423001, Roche) and α-Flag (catalogue no. F7425, MilliporeSigma). Antibodies were used at a dilution of 1:5,000 (Tris-buffered saline with Tween plus 2% non-fat milk powder).

Reporting summary

Further information on research design is available in the Nature Portfolio Reporting Summary linked to this article.

Data availability

All data are available in the main text, Supplementary Information and the listed Protein Data Bank (PDB) files: Apo-EDS1–SAG101 (PDB 4NFU); EDS1–SAG101 with ADRr-ATP (PDB 7XJP); EDS1–SAG101–NRG1A$^{WHD\text{-}LRR}$ (PDB 8YN1); and EDS1–SAG101–NRG1C (PDB 8YN0). Full versions of all gels and blots are provided in Supplementary Fig. 1. Source Data are provided with this paper.

Code availability

No custom code or mathematical algorithms were used in this study.

45. Otwinowski, Z. & Minor, W. Processing of X-ray diffraction data collected in oscillation mode. *Methods Enzymol.* **276**, 307–326 (1997).
46. Hough, M. A. & Wilson, K. S. From crystal to structure with CCP4. *Acta Crystallogr. D Struct. Biol.* **74**, 67 (2018).
47. Emsley, P. & Cowtan, K. Coot: model-building tools for molecular graphics. *Acta Crystallogr. D Struct. Biol.* **60**, 2126–2132 (2004).
48. Zheng, S. et al. MotionCor2: anisotropic correction of beam-induced motion for improved cryo-electron microscopy. *Nat. Methods* **14**, 331–332 (2017).
49. Mindell, J. A. & Grigorieff, N. Accurate determination of local defocus and specimen tilt in electron microscopy. *J. Struct. Biol.* **142**, 334–347 (2003).
50. Scheres, S. H. RELION: implementation of a Bayesian approach to cryo-EM structure determination. *J. Struct. Biol.* **180**, 519–530 (2012).
51. Scheres, S. H. Processing of structurally heterogeneous cryo-EM data in RELION. *Methods Enzymol.* **579**, 125–157 (2016).
52. Scheres, S. H. A Bayesian view on cryo-EM structure determination. *J. Mol. Biol.* **415**, 406–418 (2012).
53. Rosenthal, P. B. & Henderson, R. Optimal determination of particle orientation, absolute hand, and contrast loss in single-particle electron cryomicroscopy. *J. Mol. Biol.* **333**, 721–745 (2003).
54. Pettersen, E. F. et al. UCSF chimera – a visualization system for exploratory research and analysis. *J. Comput. Chem.* **25**, 1605–1612 (2004).
55. Adams, P. D. et al. PHENIX: a comprehensive Python-based system for macromolecular structure solution. *Acta Crystallogr. D Struct. Biol.* **66**, 213–221 (2010).

Acknowledgements We thank staff at the X-ray crystallography platform, National Protein Science Facility, Tsinghua University, and at Shanghai Synchrotron Radiation Facility, for assistance with X-ray diffraction data collection. We thank J. Wang, J. Zhao and B. Xu at the Institute of Advanced Agricultural Sciences, Peking University for provision of cryo-EM facility support. This project was supported by the Research Center for Industries of the Future at Westlake University, the National Natural Science Foundation of China (no. 32171193 to Z.H.), the National Key Research and Development Program of China (no. 2021YFA1300701 to Z.H.), the Max-Planck Society and Deutsche Forschungsgemeinschaft funding (German Research Foundation, no. SFB-1403–414786233 to J.W. and J.E.P.).

Author contributions Experimental design was the responsibility of J.C., J.E.P., Z.H., S.H. and J.W. Recombinant protein expression assays, purification, structure determination, modelling and data analysis were performed by S.H., R.S., A.J., Y.X., Y.S. and J.C. Biochemical assays were carried out by S.H., R.S., A.J., L.W., J.W., D.M., Z.W., Z.H., X.L., J.E.P. and J.C. Plant cell death assays and immunoblot analysis were undertaken by J.W., D.M. and J.E.P. All authors carried out data analysis. J.C. wrote the manuscript draft. J.E.P., Z.H., X.L., S.H., J.W. and R.S. edited the manuscript, with contributions from the other authors.

Competing interests The authors declare no competing interests.

Additional information

Supplementary information The online version contains supplementary material available at https://doi.org/10.1038/s41586-024-08521-7.

Correspondence and requests for materials should be addressed to Jane E. Parker or Jijie Chai.

Peer review information *Nature* thanks Tian-Min Fu, John Rathjen and the other, anonymous, reviewer(s) for their contribution to the peer review of this work.

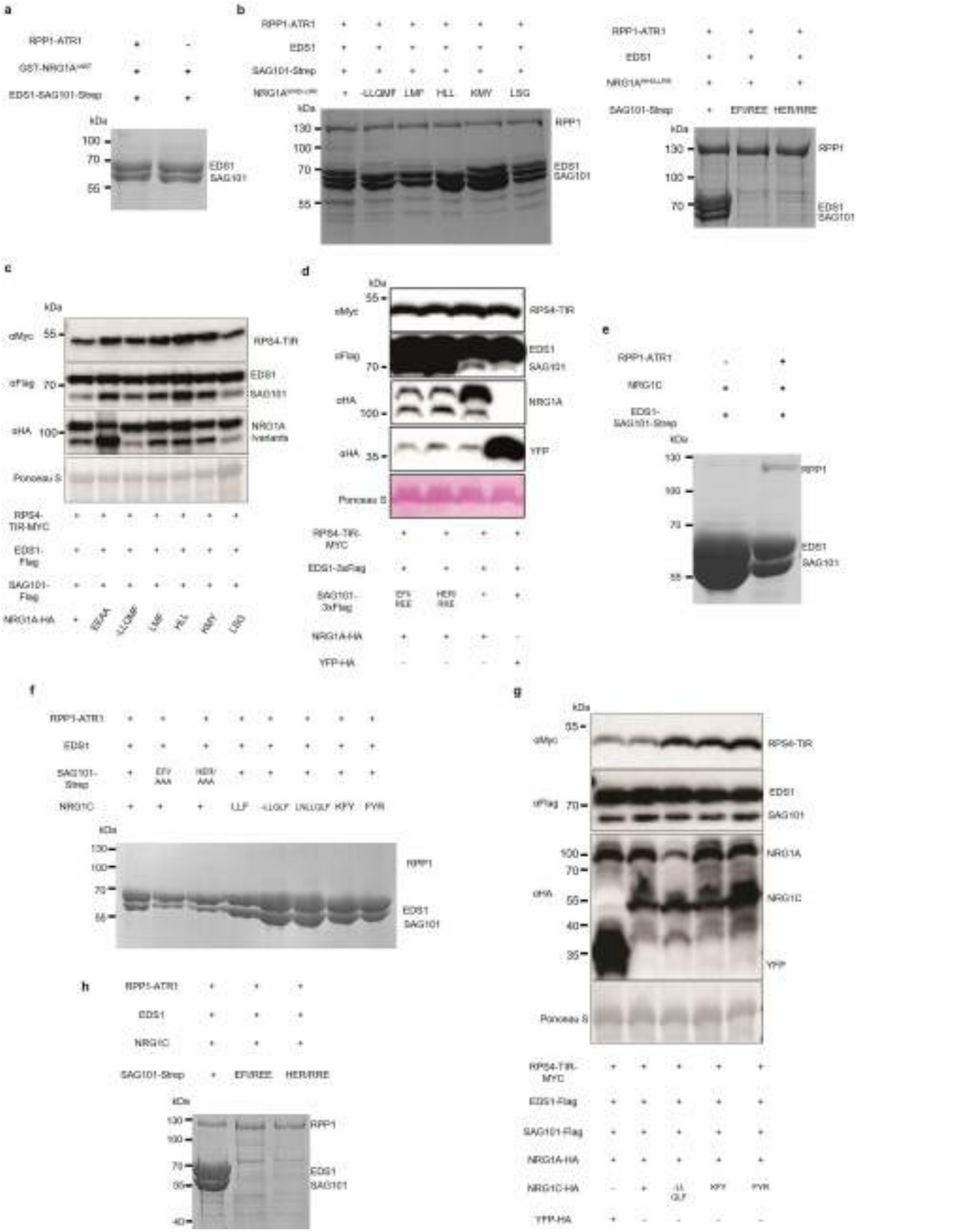

Extended Data Fig. 1 | Proteins used for pull-down assays and ion leakage measurement assays. a, **b**, **e**, **f**, **h**, Proteins used for pull-down assays in Fig. 1a (**a**), Fig. 3c (**b**), Fig. 4a (**e**), Fig. 4e (**f**) and Fig. 5b (**h**) were purified using Strep beads and analysed by SDS-PAGE. **c**, **d**, **g**, Proteins in Fig. 3d (**c**), Fig. 3e (**d**), Fig. 4f (**g**) were detected via western blot. Ponceau S served as loading control. The experiments were independently repeated three (a, b, d, e, f, g, h) or four (c) times with similar results. For gel source data, see Supplementary Fig. 1.

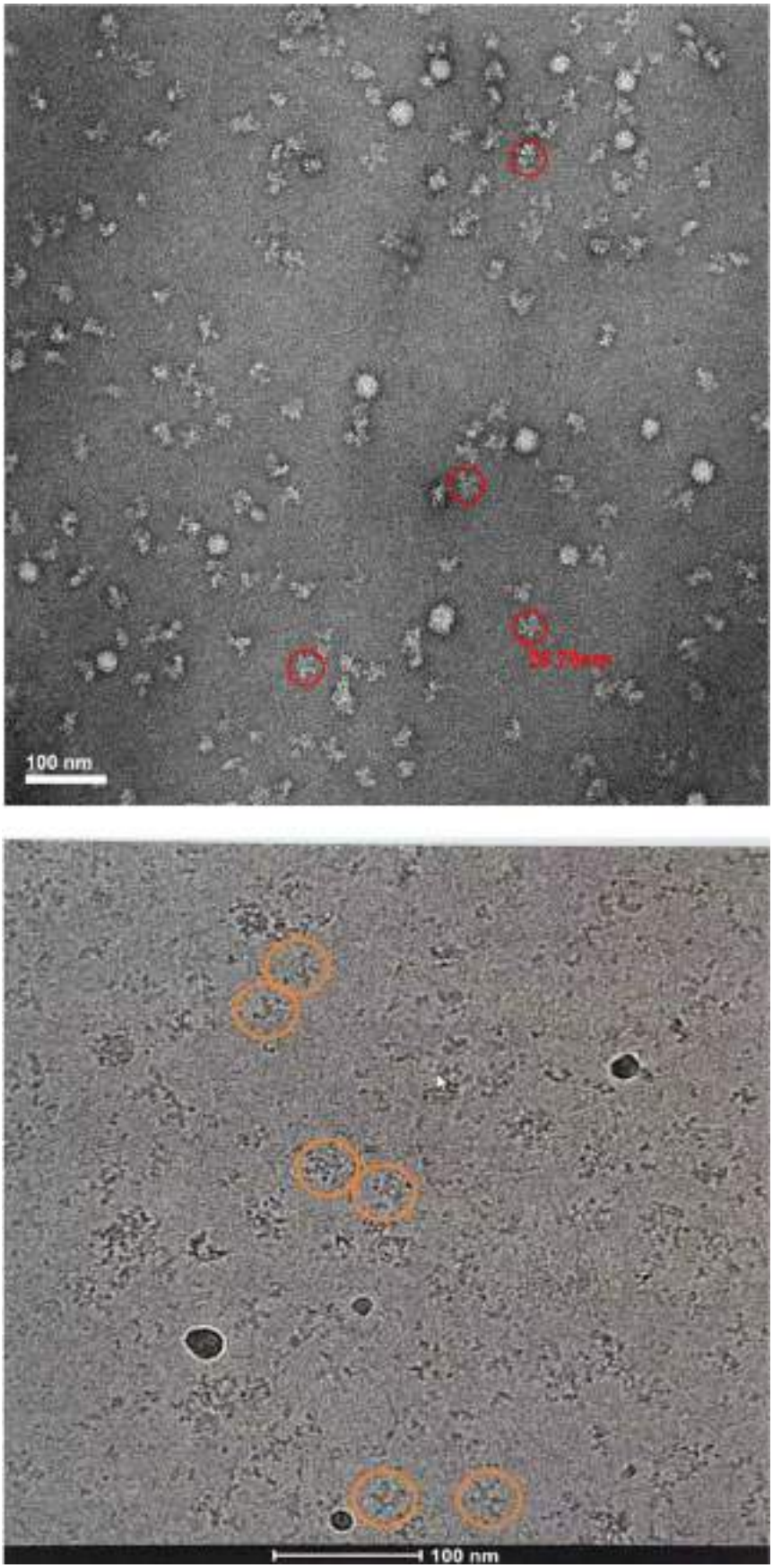

Extended Data Fig. 2 | Negative staining and cryo-EM micrographs of the purified EDS1-SAG101-NRG1A$^{\Delta N57}$ protein. The EDS1-SAG101-NRG1A protein complex was purified through affinity and size-exclusion chromatography. The peak fractions from gel filtration chromatography were used for negative staining and cryo-EM. The pentamer-like particles are highlighted in red circles (top) in negative staining and orange (bottom) in cryo-EM with a size of approximately 26 nm. Scale bar, 100 nm. Protein purification and corresponding micrograph identification were repeated three times with similar results.

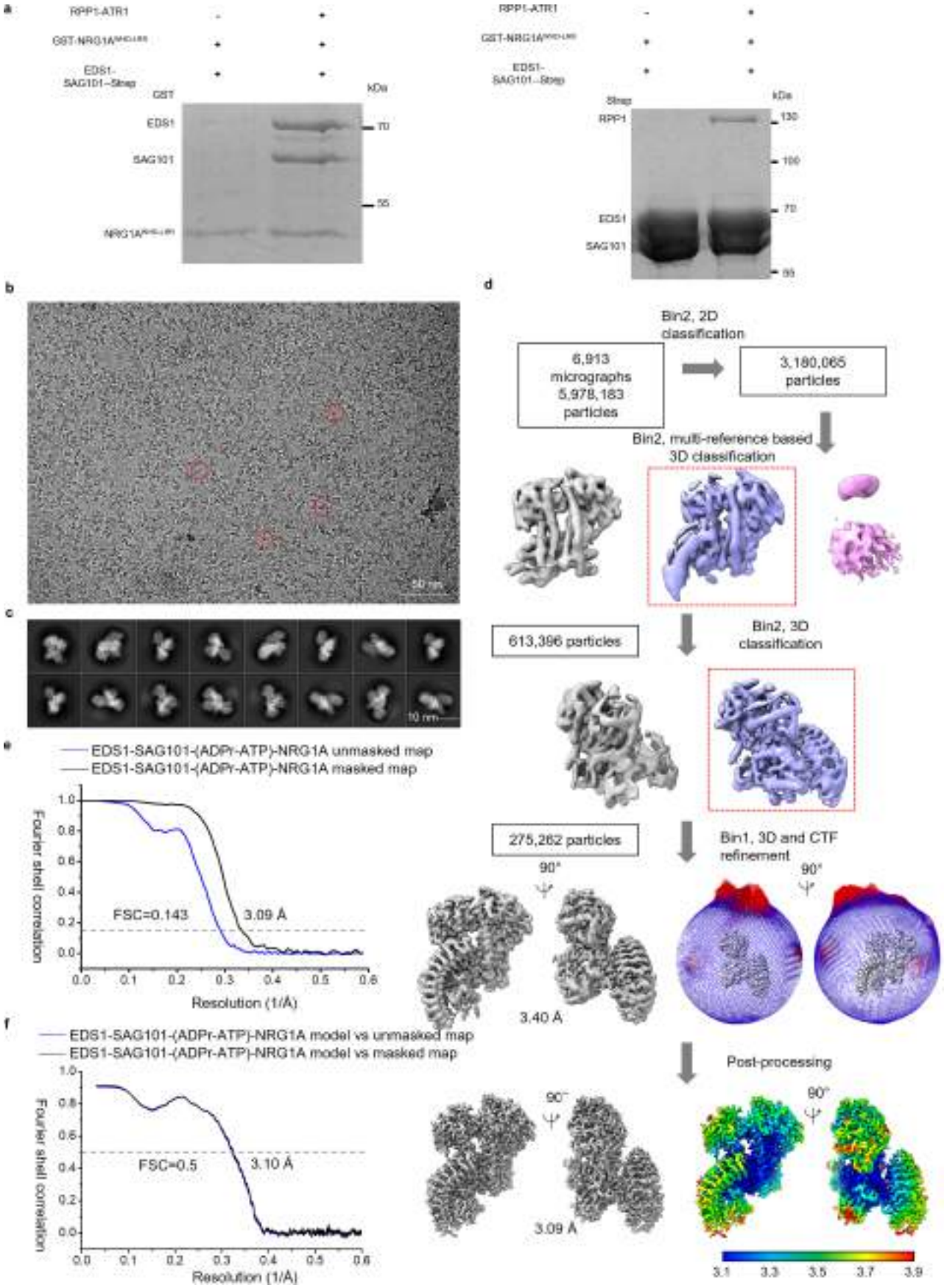

Extended Data Fig. 3 | See next page for caption.

Extended Data Fig. 3 | Cryo-EM reconstruction of the EDS1-SAG101-NRG1A$^{WHD-LRR}$ complex. a, Reconstitution of EDS1-SAG101-NRG1A$^{WHD-LRR}$. NRG1A$^{WHD-LRR}$ was co-expressed with EDS1, SAG101, RPP1 and ATR1 in insect cells. The protein complex was purified using GS4B beads, following the Strep beads, and analysed by SDS-PAGE. The experiment was repeated three times with similar results. For gel source data, see Supplementary Fig. 1. **b**, A representative cryo-EM micrograph selected from 6,913 micrographs of the EDS1-SAG101-NRG1A$^{WHD-LRR}$ complex. **c**, Representative views of 2D class averages of the EDS1-SAG101-NRG1A$^{WHD-LRR}$ complex. **d**, The cryo-EM image processing workflow for the EDS1-SAG101-NRG1A$^{WHD-LRR}$ complex. **e**, FSC curves at 0.143 of the final reconstructions of the EDS1-SAG101-NRG1A$^{WHD-LRR}$ complex unmasked (blue) or masked (black). **f**, FSC curves at 0.5 for model refined against the final masked map (black) and the unmasked map (blue).

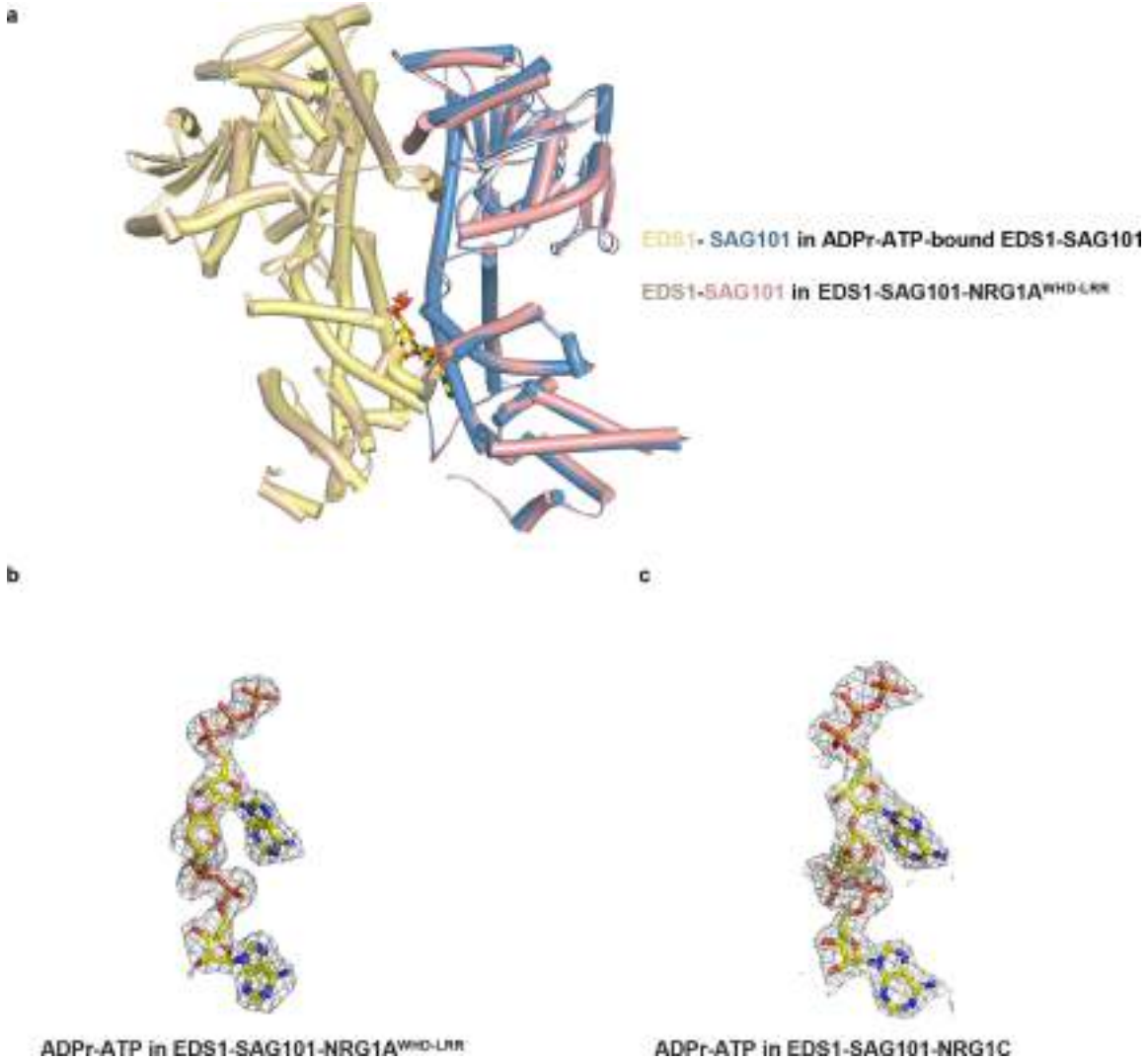

Extended Data Fig. 4 | Structural comparison of ADPr-ATP-bound EDS1-SAG101 with EDS1-SAG101-NRG1A$^{WHD-LRR}$ and EDS1-SAG101-NRG1C. a, The cryo-EM structures of ADPr-ATP-bound EDS1-SAG101 (PDB code: 7XJP) and EDS1-SAG101 from EDS1-SAG101-NRG1A$^{WHD-LRR}$ were aligned with PyMOL. Colour codes are shown as indicated. **b**, ADPr-ATP of the cryo-EM structure of EDS1-SAG101-NRG1A$^{WHD-LRR}$ complex. **c**, ADPr-ATP of the crystal structure of EDS1-SAG101-NRG1C. ADPr-ATP is shown in stick. The cryo-EM density (**b**) and the electron density (**c**) surrounding the small molecule are shown in grey mesh. The map was contoured at 1.2 sigma in PyMOL.

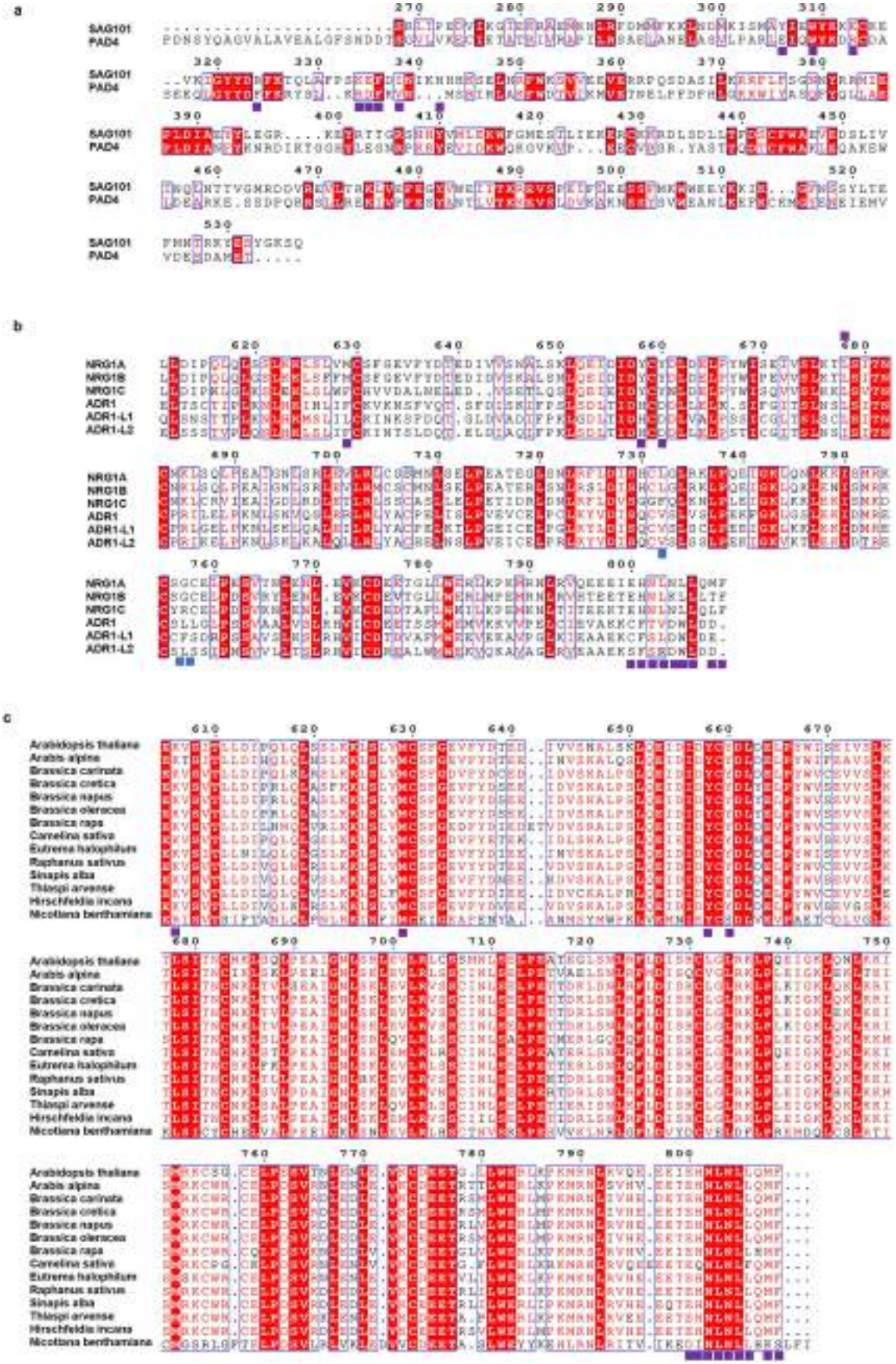

Extended Data Fig. 5 | See next page for caption.

Extended Data Fig. 5 | Sequence alignment of *Arabidopsis* PAD4 with SAG101, NRG1 family proteins with ADR1 family proteins, and NRG1 from different plant species. a, Amino acid sequence alignment among *Arabidopsis* PAD4 and SAG101. **b**, Amino acid sequence alignment among NRG1 and ADR1 family proteins in *Arabidopsis*. **c**, Amino acid sequence alignment of NRG1A from different plant species. Putative NRG1A homologues of other species as indicated were obtained from NCBI (National Library of Medicine) using *A. thaliana* NRG1A sequence as a query. Except *Nicotiana benthamiana*, other species all belong to *Brassicaceae*. Clustal Omega was used for the sequence alignment. In **a**-**c**, residues of SAG101 and NRG1A involved in interacting are marked with solid purple squares at the bottom. Bulkier residues of NRG1C interacting with EDS1-SAG101 are marked with solid blue squares at the bottom.

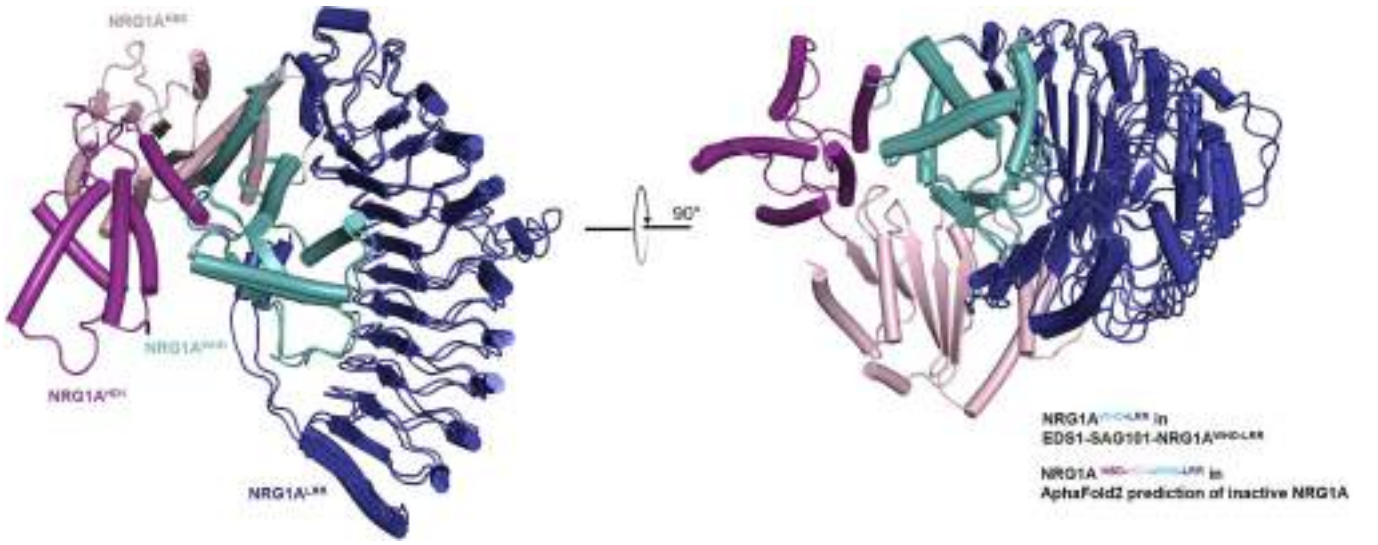

Extended Data Fig. 6 | Structure comparisons of the AlphaFold2-predicted structure of inactive NRG1A$^{NOD\text{-}LRR}$ with experimental structures. a, The AlphaFold2-predicted structure of inactive NRG1A$^{NOD\text{-}LRR}$ resembles that of the corresponding segment of the inactive ZAR1$^{NOD\text{-}LRR}$. The cryo-EM structure of inactive ZAR1-RKS1 (PDB code: 6J5W) and Alphafold2-predicted structure of inactive NRG1A$^{NOD\text{-}LRR}$ were aligned with PyMOL. **b**, The AlphaFold2-predicted structure of inactive NRG1A$^{NOD\text{-}LRR}$ and NRG1A$^{WHD\text{-}LRR}$ of EDS1-SAG101-NRG1A$^{WHD\text{-}LRR}$ were aligned with PyMOL. Structures were shown in cartoon representations. Colour codes are shown as indicated.

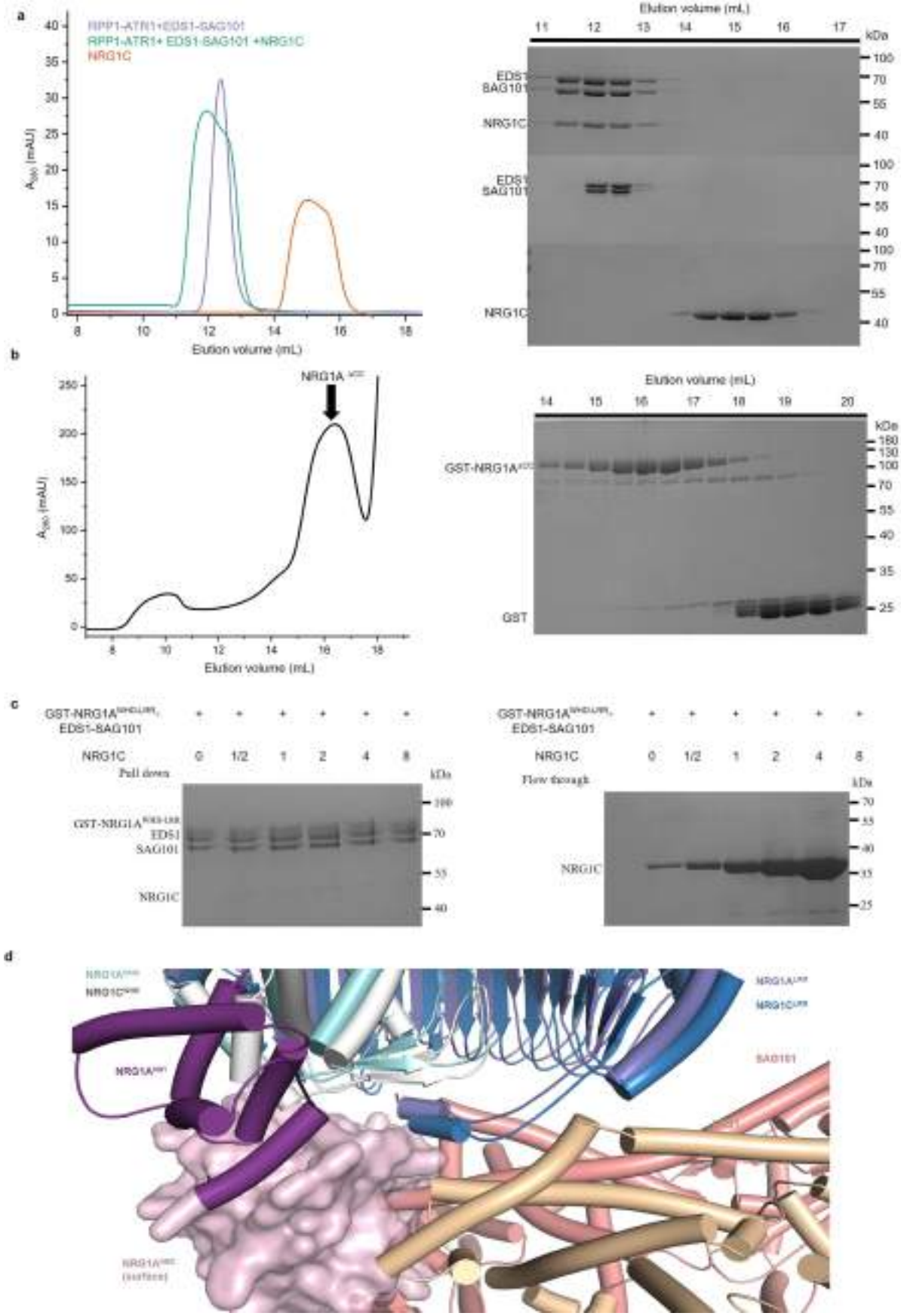

Extended Data Fig. 7 | See next page for caption.

Extended Data Fig. 7 | Competition between NRG1A and NRG1C for the interaction with the EDS1-SAG101 complex. a, EDS1-SAG101 and NRG1C form a monomeric ternary complex in gel filtration. Shown in the left are gel filtration profiles (Superdex 200 Increase 10/300) of EDS1-SAG101 (purple), NRG1C (red), and EDS1-SAG101-NRG1C (green) proteins. A_{280}, absorbance at 280 nm; mAU, milli-absorbance units. Peak fractions in the left were visualized by SDS-PAGE followed by Coomassie blue staining and are shown on the right. **b**, Purification of NRG1A$^{\Delta CC}$ protein. N terminal GST tagged NRG1A$^{\Delta CC}$ (residues 160-809) was expressed in insect cells. GST beads were used to purify proteins, which were further purified by Superose 6 Increase 10/300 GL. Left: a gel filtration profile of NRG1A$^{\Delta CC}$. Right: SDS-PAGE analysis of peak fractions. **c**, NRG1C fails to efficiently outcompete NRG1A$^{WHD\text{-}LRR}$ in EDS1-SAG101- NRG1A$^{WHD\text{-}LRR}$. 0.08 µmol the EDS1-SAG101-NRG1A$^{WHD\text{-}LRR}$ (with a GST tag) complex protein was incubated with a varying amount of NRG1C (0, 0.04, 0.08, 0.16, 0.32, 0.64 µmol). The mixture was flowed through the Strep beads. After extensive washing, the beads were analysed by SDS-PAGE. In **a**-**c**, the experiments were repeated three times with similar results. For gel source data, see Supplementary Fig. 1. **d**, Structural comparison of EDS1-SAG101-NRG1C with AlphaFold2-predicted EDS1-SAG101-NRG1A$^{NOD\text{-}LRR}$. The cryo-EM structure of EDS1-SAG101-NRG1C (PDB code: 8YN0) was aligned with AlphaFold2-predicted EDS1-SAG101-NRG1A$^{NOD\text{-}LRR}$ in PyMOL. The NBD of NRG1A is shown in surface and others in cartoon representation. The NBD of NRG1A clashes with EP domains of EDS1-SAG101.

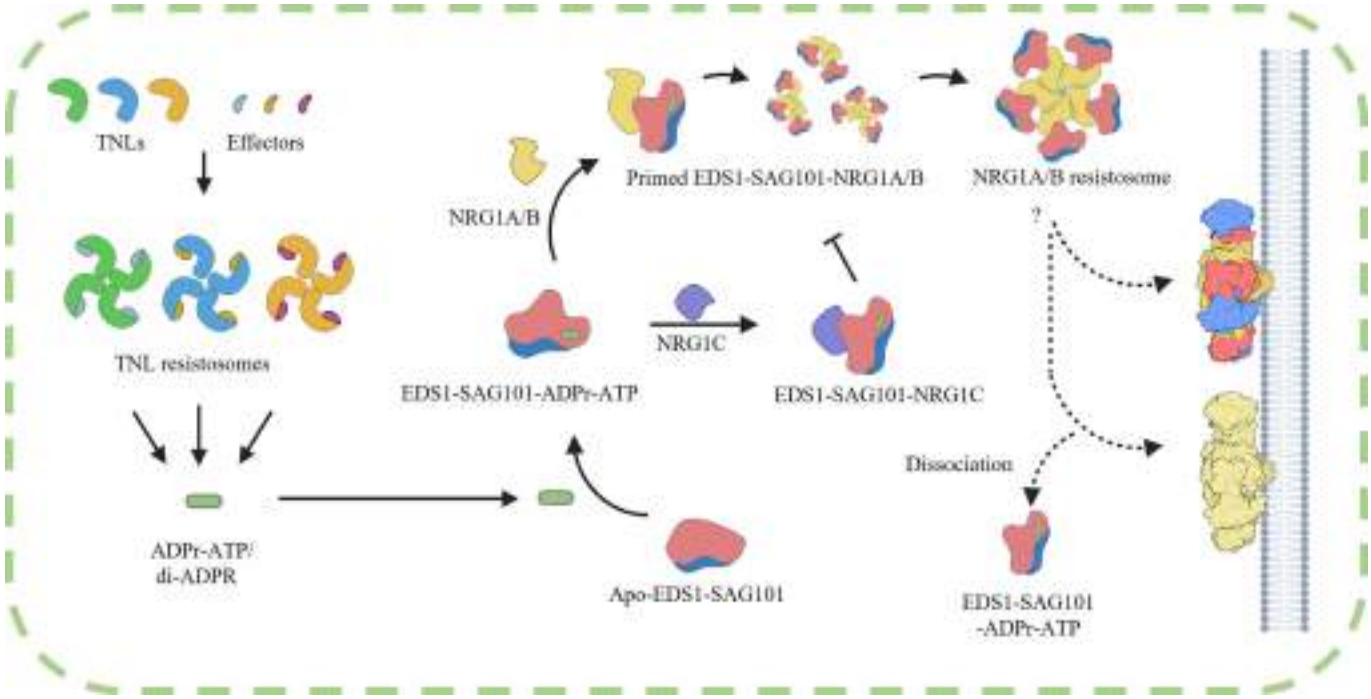

Extended Data Fig. 8 | Working model on activation and regulation of the EDS1-SAG101-NRG1 signaling branch in *Arabidopsis*. TNLs form resistosomes upon recognizing their corresponding pathogen effectors. These resistosomes catalyse the production of the nucleotide-derived small molecules ADPr-ATP and di-ADPR, which bind to the apo-EDS1-SAG101 complex. Binding of these small molecules induces conformational changes in EDS1-SAG101, which are recognized by NRG1 family proteins, including NRG1A, NRG1B, and NRG1C. This results in the oligomerization of EDS1-SAG101-NRG1A/B and the assembly of NRG1A/B resistosomes in plasma membrane (and/or other endo-membranes), activating their Ca^{2+}-permeable channel activity to initiate ETI signalling. NRG1C, which lacks the NOD module, forms monomeric complex with EDS1-SAG101. Because of its higher affinity than inactive NRG1A/B, NRG1C efficiently outcompetes NRG1A/B for binding to the ADPr-ATP/di-ADPR-bound EDS1-SAG101 complex, sequestering the activated EDS1-SAG101 from inactive NRG1A/B and negatively regulating NRG1A/B immune signalling.

Extended Data Table 1 | Cryo-EM statistics and model refinement for EDS1-SAG101-NRG1A$^{WHD-LRR}$

	EDS1-SAG101-NRG1A$^{WHD-LRR}$
PDB ID	8YN1
EMDB ID	EMD-39411
Data collection and processing	
Microscope	Thermo Scientific Krios G4
Voltage (kV)	300
Detector	Gatan K3 Cameras
Magnification	105,000
Pixel size (Å)	0.425
Total electron dose ($e^-/Å^2$)	50
Number of frames collected	40
Exposure rate (e^-/pixel/sec)	15
Automation software	EPU 2
Defocus range (μm)	-1.0~-2.0
Micrographs collected	6,930
Micrographs used	6,913
Reconstruction	
Software	RELION 4.0
Total extraced particles	5,978,183
Number of particles used for refinement	275,262
Symmetry	C1
Resolution range (Å)	2.92~4.67
Resolution (Å) after refinement (FSC=0.143)	3.40
Resolution (Å) after post-processing (FSC=0.143)	3.09
Map sharpening B-factor ($Å^2$)	-120
Refinement and validation	
Software	phenix.real space refine
Model resolution (Å) (FSC=0.5)	3.10
Model composition	
Non-hydrogen atoms	12,181
Protein residues	1,495
Ligand atoms	132
Map-model CC (mask/box)	0.79/0.77
Mean B factors ($Å^2$, protein/ligand)	11.26/14.80
R.M.S deviations	
Bonds lengths (Å)	0.008
Bonds angles (°)	0.874
MolProbity overall score	1.81
All-atom clashscore	7.90
Rotamer outliers (%)	0.00
Cβ outliers (%)	0.00
EMRinger score	3.14
Ramachandran plot statistics	
Preferred (%)	95.14
Allowed (%)	4.86
Outlier (%)	0.00

Extended Data Table 2 | Summary of crystallography analysis of EDS1-SAG101-NRG1C

Data collection	
Data set	EDS1-SAG101-NRG1C
PDB code	8YN0
Wavelength (Å)	0.979
Resolution (Å)	50-2.50 (2.54-2.50)
Space group	P 2_1
Cell dimensions	91.52 154.91 171.11
(Å/degree)	90.00 89.69 90.00
Unique reflections	159,460 (7,943)
Completeness (%)	96.1 (95.8)
Rmeas (%)	15.0 (99.0)
Rpim (%)	8.3 (54.7)
Redundancy	3.0 (2.9)
Average $I/\sigma(I)$	9.1 (1.3)
Wilson B value (Å^2)	45.59
Statistics for Refinement	
Resolution (Å)	39.77-2.49 (2.581-2.49)
Rwork (%)	19.9 (28.2)
Rfree (%)	23.8 (33.3)
Reflections used	158,978 (15,172)
R.m.s.d.	
Bond (degree)	1.420
Length (Å)	0.010
No. of atoms	26,048
proteins	25,209
ligands	132
waters	707
Average B factors (Å^2)	55.1
proteins	55.4
ligands	39.1
waters	50.1
Ramachandran plot	
Favored region (%)	95.89
Allowed region (%)	4.11
Outliers (%)	0.00

$R_{means}=\Sigma_h\sqrt{[n/(n-1)]}\Sigma_i|I_{h,i}-\langle I_h\rangle|/\Sigma_h\Sigma_i I_{h,i}$, where I_h is the mean intensity of the i observations of symmetry related reflections of h. $R_{factor}=\Sigma|F_{obs}-F_{calc}|/\Sigma F_{obs}$, where $F_{obs}=F_h$, and F_{calc} is the calculated protein structure factor from the atomic model. R_{work} was calculated with 95.0% of the reflections. R_{free} was calculated with 5.0% of the reflections which were randomly selected and were not used for structure refinement. R.m.s.d. (root-mean-square error) in bond lengths and angles are the deviations from ideal values. Values in parentheses correspond to the last resolution shell.

nature portfolio

Corresponding author(s): Jijie Chai
Jane E. Parker

Last updated by author(s): Apr 30, 2024

Reporting Summary

Nature Portfolio wishes to improve the reproducibility of the work that we publish. This form provides structure for consistency and transparency in reporting. For further information on Nature Portfolio policies, see our Editorial Policies and the Editorial Policy Checklist.

Statistics

For all statistical analyses, confirm that the following items are present in the figure legend, table legend, main text, or Methods section.

n/a	Confirmed
☐	☒ The exact sample size (*n*) for each experimental group/condition, given as a discrete number and unit of measurement
☐	☒ A statement on whether measurements were taken from distinct samples or whether the same sample was measured repeatedly
☐	☒ The statistical test(s) used AND whether they are one- or two-sided *Only common tests should be described solely by name; describe more complex techniques in the Methods section.*
☒	☐ A description of all covariates tested
☒	☐ A description of any assumptions or corrections, such as tests of normality and adjustment for multiple comparisons
☐	☒ A full description of the statistical parameters including central tendency (e.g. means) or other basic estimates (e.g. regression coefficient) AND variation (e.g. standard deviation) or associated estimates of uncertainty (e.g. confidence intervals)
☐	☒ For null hypothesis testing, the test statistic (e.g. *F*, *t*, *r*) with confidence intervals, effect sizes, degrees of freedom and *P* value noted *Give P values as exact values whenever suitable.*
☒	☐ For Bayesian analysis, information on the choice of priors and Markov chain Monte Carlo settings
☒	☐ For hierarchical and complex designs, identification of the appropriate level for tests and full reporting of outcomes
☒	☐ Estimates of effect sizes (e.g. Cohen's *d*, Pearson's *r*), indicating how they were calculated

Our web collection on statistics for biologists contains articles on many of the points above.

Software and code

Policy information about availability of computer code

Data collection	BL19U1,EPU (Thermo Fisher Scientific) 2.8.1.10
Data analysis	RELION 4.0, MotionCor2, CTFFIND4, CCP4i 7.1, Phenix 1.20 , Chimera 1.15, Coot 0.9.6, Pymol 2.4.0, HKL2000 v718, MicroCal PEAQ-ITC, R 4.2.2

For manuscripts utilizing custom algorithms or software that are central to the research but not yet described in published literature, software must be made available to editors and reviewers. We strongly encourage code deposition in a community repository (e.g. GitHub). See the Nature Portfolio guidelines for submitting code & software for further information.

Data

Policy information about availability of data

All manuscripts must include a data availability statement. This statement should provide the following information, where applicable:

- Accession codes, unique identifiers, or web links for publicly available datasets
- A description of any restrictions on data availability
- For clinical datasets or third party data, please ensure that the statement adheres to our policy

All data are available in the main text, supplementary materials, or the listed Protein Data Bank (PDB) files, Apo-EDS1-SAG101 (PDB ID: 4NFU), EDS1-SAG101 with ADRr-ATP (PDB ID: 7XJP), EDS1-SAG101-NRG1AWHD-LRR (PDB ID: 8YN1) and EDS1-SAG101-NRG1C (PDB ID: 8YN0). Full version of all gels and blots are provided in Supplementary information Fig. 1. Source statistical data are provided with this paper.

Research involving human participants, their data, or biological material

Policy information about studies with human participants or human data. See also policy information about sex, gender (identity/presentation), and sexual orientation and race, ethnicity and racism.

Reporting on sex and gender	not applicable
Reporting on race, ethnicity, or other socially relevant groupings	not applicable
Population characteristics	not applicable
Recruitment	not applicable
Ethics oversight	not applicable

Note that full information on the approval of the study protocol must also be provided in the manuscript.

Field-specific reporting

Please select the one below that is the best fit for your research. If you are not sure, read the appropriate sections before making your selection.

☒ Life sciences ☐ Behavioural & social sciences ☐ Ecological, evolutionary & environmental sciences

For a reference copy of the document with all sections, see nature.com/documents/nr-reporting-summary-flat.pdf

Life sciences study design

All studies must disclose on these points even when the disclosure is negative.

Sample size	Sample size was determined based on previous publications on similar experiments: cell death assays and ion leakage measurement：Sun, X. et al. Pathogen effector recognition-dependent association of NRG1 with EDS1 and SAG101 in TNL receptor immunity. Nature Communications 12, 3335 (2021).
Data exclusions	Data exclusion for particles in bad 2D or 3D classes with no defined features was a standard processing for EM data.
Replication	Each experiments were successfully repeated independently at least twice or three times, and the number of independent experiments is indicated in the figure legends.
Randomization	For each independent experiments, Nicotiana benthamiana leaves were selected with similar sizes and at the same position in each plant to minimize the side effects caused by plant growth. These plants were randomly assigned to the treatment and control groups with no formal randomization techniques.
Blinding	The cell death, ion leakage measurement and western blot assays were recorded in a blind way. Experiment results are not subjective.

Reporting for specific materials, systems and methods

We require information from authors about some types of materials, experimental systems and methods used in many studies. Here, indicate whether each material, system or method listed is relevant to your study. If you are not sure if a list item applies to your research, read the appropriate section before selecting a response.

Materials & experimental systems

n/a	Involved in the study
☐	☒ Antibodies
☐	☒ Eukaryotic cell lines
☒	☐ Palaeontology and archaeology
☒	☐ Animals and other organisms
☒	☐ Clinical data
☒	☐ Dual use research of concern
☐	☒ Plants

Methods

n/a	Involved in the study
☒	☐ ChIP-seq
☒	☐ Flow cytometry
☒	☐ MRI-based neuroimaging

Antibodies

Antibodies used	Antibodies used for immunoblotting were α-MYC (71D10, Cell Signaling), α-HA (11867423001, Roche) and α-Flag (F7425, MiliporeSigma). Antibodies were used in dilution 1:5,000 (TBST with 2% non-fat milk powder).
Validation	The antibody we used are all from mature commercial company(Cell Signaling, Roche and MiliporeSigma). The validation experiments can be found on their company website. α-MYC: https://www.cellsignal.cn/products/primary-antibodies/myc-tag-71d10-rabbit-mab/2278. α-HA: https://www.sigmaaldrich.cn/deepweb/assets/sigmaaldrich/product/documents/244/078/roahaha.pdf. α-Flag: https://www.sigmaaldrich.com/specification-sheets/447/086/F7425-BULK_____SIGMA____.pdf

Eukaryotic cell lines

Policy information about cell lines and Sex and Gender in Research

Cell line source(s)	Sf21 cell lines from Thermo Fischer Scientific. https://www.thermofisher.cn/order/catalog/product/11497013?SID=srch-srp-11497013
Authentication	Sf21 cell lines were verified by manufacturer's website and Identity of these cell lines were frequently checked by their morphological features. https://www.thermofisher.cn/order/catalog/product/11497013?SID=srch-srp-11497013
Mycoplasma contamination	Sf21 cell lines were tested negative for mycoplasma contamination by Mycoplasma qPCR Detection Assay. https://www.thermofisher.cn/document-connect/document-connect.html?url=https://assets.thermofisher.cn/TFS-Assets%2Fcertificate%2FCBD%2FCOA%2FCOA_11497013_2656261_1.pdf
Commonly misidentified lines (See ICLAC register)	No commonly misidentified cell lines are used in this study.

Dual use research of concern

Policy information about dual use research of concern

Hazards

Could the accidental, deliberate or reckless misuse of agents or technologies generated in the work, or the application of information presented in the manuscript, pose a threat to:

No	Yes	
☒	☐	Public health
☒	☐	National security
☒	☐	Crops and/or livestock
☒	☐	Ecosystems
☒	☐	Any other significant area

Experiments of concern

Does the work involve any of these experiments of concern:

No	Yes	
☒	☐	Demonstrate how to render a vaccine ineffective
☒	☐	Confer resistance to therapeutically useful antibiotics or antiviral agents
☒	☐	Enhance the virulence of a pathogen or render a nonpathogen virulent
☒	☐	Increase transmissibility of a pathogen
☒	☐	Alter the host range of a pathogen
☒	☐	Enable evasion of diagnostic/detection modalities
☒	☐	Enable the weaponization of a biological agent or toxin
☒	☐	Any other potentially harmful combination of experiments and agents

Plants

Seed stocks	N. benthamiana-epss quadruple knockout mutant (eds1a pad4 sag101a sag101b) was generated and provided by Jane. E. Parker lab.
Novel plant genotypes	No novel plant genotype is generated.
Authentication	N. benthamiana-epss was verified by genome DNA sequencing.